Chem Soc Rev

Phonon and Raman scattering of two-dimensional transition metal dichalcogenides from monolayer, multilayer to bulk material

SCHOLARONE™
Manuscripts

ARTICLE TYPE

Phonon and Raman scattering of two-dimensional transition metal dichalcogenides from monolayer, multilayer to bulk material

Xin Zhang, Xiao-Fen Qiao, Wei Shi, Jiang-Bin Wu, De-Sheng Jiang and Ping-Heng Tan[*]

Two-dimensional (2-D) transition metal dichalcogenide (TMD) nanosheets exhibit remarkable electronic and optical properties. The 2-D features, sizable bandgaps and recent advances in synthesis, characterization and device fabrication of the representative MoS_2, WS_2, WSe_2 and $MoSe_2$ make TMDs much attractive in nanoelectronics and optoelectronics. Similar to graphite and graphene, atoms within each layer in 2-D TMDs are combined together by covalent bonds, while van der Waals interactions keep the layers together. This makes the physical and chemical properties of 2-D TMDs layer-dependent. In this review, we discuss the basic lattice vibrations of 2-D TMDs from monolayer, multilayer to bulk material, such as high-frequency optical phonons, interlayer shear and layer breathing phonons, Raman selection rule, layer-number evolution of phonons, multiple phonon replica and phonons at the edge of Brillouin zone. The extensive capabilities of Raman spectroscopy are demonstrated in investigating their properties, such as interlayer coupling, spin-obit splitting and external perturbations. The interlayer vibrational modes are further utilized in rapid and substrate-free characterizations of layer number for multilayer TMDs and in probing interface coupling in TMD heterostructures. Raman spectroscopy with great successes in studying TMD nanosheets paves the way to experiments on other 2-D crystals and related van der Waals heterostructures.

1 Introduction

The fast progress of graphene research, fueled by the unique properties of this two-dimensional (2-D) material, stimulated scientists' interests on other 2-D crystals.[1–6] Beyond graphene, several representative 2-D crystals have been obtained experimentally by similar methods, such as BN, MoS_2, $NbSe_2$, Bi_2Te_3, Bi_2Se_3, $Bi_2Sr_2CaCu_2O_x$, etc.[1] Actually, the library of the original 2-D crystals is very rich, including many naturally-occurred layered materials, such as a wide range of minerals, transition metal oxides and transition metal dichalcogenides (TMDs).[7] The capability of preparing/growing different families of 2-D crystals will further enhance tremendously the library of materials that one can obtain and thus allow one to explore the fascinating unusual physics in two dimension.[1] Recently, 2-D TMDs, such as MoS_2, $MoSe_2$, WS_2 and WSe_2, have attracted considerable attention due to their unique properties and their potentials in (opto-)electronics.[8–16] Those 2-D crystals can be grown or mechanically exfoliated down to the monolayer like the exfoliation of graphene. However, in contrast to graphite and graphene, TMDs consist of more than one atomic element (as shown in the case of MoS_2 in Fig.1(a), where one Mo plane sandwiched by two S planes), which makes their lat-

tice dynamics more complex than that in multilayer (ML) graphene,[17] including the symmetry, force constants and frequency trends varying with thickness of flakes.[18–20] Further, in comparison to the bulk form, monolayer (1L) and few-layer (FL) TMDs show very distinctive physical properties, particularly in lattice dynamics, electronic structure and optical properties.

Many TMDs show a graphene-like layered structure with the single carbon atomic layer replaced by the repeat unit of X-M-X, where M is a transition metal of group VI (Mo or W) and X is a chalcogens (S, Se or Te). More than 40 different types of TMDs occur, dependent on the combination of chalcogens and metals. The chalcogen atoms (S) in two hexagonal planes are separated by a plane of metal atoms (Mo), as shown in the case of 1L-MoS_2 in Fig.1(a). As indicated by the black triangular prism in Fig.1(a), the Mo atom has trigonal prismatic coordination, where the upper triangle is obtained by mirroring the bottom triangle. This repeat unit stacking along *c* axis will form two different polytypes, i.e., 2H (hexagonal symmetry, two X-M-X layers per repeat unit, trigonal prismatic coordination, H stands for hexagonal) and 3R (rhombohedral symmetry, three X-M-X layers per repeat unit, trigonal prismatic coordination, R stands for rhombohedral).[4] Actually, the site of metal atom can also has octahedral coordination, where the upper triangle is inversion of the bottom triangle, which gives the third polytype of 1T[4,22,23] (tetragonal symmetry, one X-M-X unit in the unit cell, octahedral coordination, T stands for

State Key Laboratory of Superlattices and Microstructures, Institute of Semiconductors, Chinese Academy of Sciences, Beijing 100083, China. E-mail: phtan@semi.ac.cn
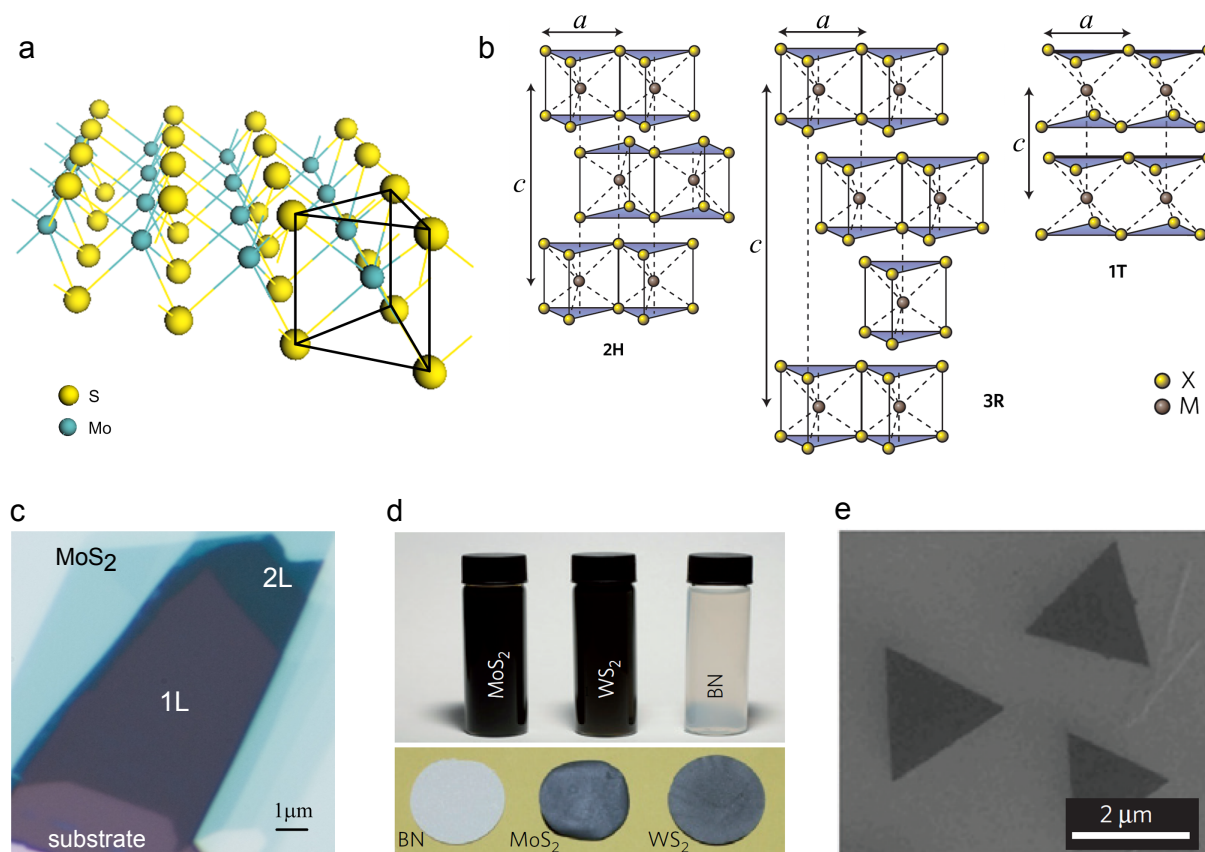
Fig. 1 (a) Three-dimensional structure schematic of 1L-MoS$_2$. The triangular prism denoted by black lines represents trigonal prismatic coordination of Mo atoms. (b) Schematics of the three typical structure polytypes of MX$_2$: 2H, 3R and 1T. *a* and *c* represent lattice constants. Reproduced with permission from ref.4. Copyright 2012, Nature Publishing Group. (c) Optical image of 1L- and 2L- MoS$_2$ obtained by micro-mechanical cleavage. (d) Stable suspensions of MoS$_2$, WS$_2$ and BN from liquid-phase exfoliation in solvents (top), and thin films derived from vacuum filtration of these suspensions (bottom). Reproduced with permission from ref.21. Copyright 2013, American Association for the Advancement of Science. (e) SEM images of triangle MoS$_2$ thin films by vapour phase growth. Reproduced with permission from ref.21. Copyright 2013, Nature Publishing Group.

trigonal). The schematics of the three structure polytypes are depicted in Fig.1(b).[4] Difference between symmetry of trigonal prismatic and octahedral coordination for metal atoms can result totally different electronic structure in its monolayer. For example, monolayer of 2H-MoS$_2$ is semiconducting,[8,9] while that of 1T-MoS$_2$ is metallic.[23,24] Recently, monolayer of 1T-MoS$_2$ obtained by intercalation with alkali metals cause a transition to 2H-MoS$_2$ by annealing at 300°C, which is further verified by the re-emergence of bandgap photoluminescence (PL).[22] The symmetry difference between monolayer of 2H-MX$_2$/3R-MX$_2$ (with point group D_{3h}) and 1T-MX$_2$ (with point group D_{3d}) can be differentiated by Raman analysis.[25] Here, we mainly focus on 2H-MX$_2$ and bulk 2H-MX$_2$ is simply denoted as bulk MX$_2$ if without any specification.

Great advances have been demonstrated in MoS$_2$, which is gradually expanding to other TMDs. Most TMDs are indirect-gap semiconductors in bulk, but undergo transitions into direct-gap semiconductors when thinned down to the monolayer.[8,9,26] This can be probed by a variety of spectroscopic tools.[8,9,26–31] For example, as an indirect-gap material, bandgap PL in bulk 2H-MoS$_2$ is very weak due to its phonon-assisted process and is known to have negligible quantum yield. Appreciable PL is observed in FL MoS$_2$ and surprisingly bright PL is detected in 1L-MoS$_2$, which is indicative of being a direct-gap semiconductor.[8,9] Indirect-to-direct transition is attributed to the absence of the weak interlayer coupling in monolayer,[8,9,32] which was directly verified in FL-MoSe$_2$ via interlayer thermal expansion.[33] The direct bandgap of monolayer TMDs promises the high performance in the optoelectronic applications, such as transistors with an extra-high on/off ratio at room temperature.[10] Two peaks (A and B) are observed in the absorption spectra of 1L- and 2L- MoS$_2$, cor-

responding to transitions between split valence bands (VBs) and conduction band (CBs).[8] The energy splitting between A and B in bulk MoS_2 arises from combined effect of interlayer coupling and spin-orbit coupling (SOC), but solely comes from SOC in 1L-MoS_2 due to the absence of interlayer coupling.[8] Further, coupled spin and valley in 1L-MoS_2 due to strong SOC and inversion symmetry breaking introduce new controllable degree of freedom beyond charge and spin, leading to valleytronics.[11–16] An excited electron will attract a hole by Coulomb interaction to form a bound state (called exciton) with bound energy levels lying in bandgap region. This excitonic effect is significantly enhanced in low dimensional materials owing to strong spatial confinement and reduced screening effect.[34–39] Thus, as a 2-D material, 1L-MX_2 is expected to have a strong excitonic effect with a large exciton binding energy of $\sim$ 0.5-1.0 eV,[40–43] which will significantly influence its optical properties. In addition, one-dimensional nonlinear optical edge states are observed at the edge of 1L-MoS_2, which allows direct optical imaging of the atomic edges and boundaries of a 2-D material.[44]

Various methods were developed to obtain uniform, high-purity, thickness-controlled and large-area TMDs monolayers, which can be mainly divided into two categories: exfoliation from parent bulk crystals and chemical vapor deposition (CVD) on substrates. The coupling by weak van der Waals forces between the repeat unit X-M-X of bulk TMDs allows the crystal to be readily cleaved along the layer surface. Methods inheriting from community of graphene, like micro-mechanical cleavage,[18,45] liquid-phase exfoliation[3,46] and exfoliation by intercalation with ionic species[22] had been widely used in preparing monolayer TMDs. Samples obtained by micro-mechanical cleavage exhibit high crystal quality but need to be supported on substrates (e.g., SiO_2/Si as shown in Fig.1(c)) for optical identification.[47,48] The liquid-phase preparations of MX_2 (Fig.1(d)) are promising, which permits composites and hybrids of different MX_2.[3,49] The thickness and size of thin layers cannot be well-controlled in comparison with above exfoliation processes. Inspired by CVD of large-area graphene on copper,[50] several CVD methods based on insulating substrates have recently been reported.[4,5,51,52] The CVD growth offers TMD monolayers the possibilities for wafer-scale fabrication of electronic and optoelectronic devices.[4,5]

An ideal tool for fundamental research and material characterization should be fast and non-destructive, offer high spectral and spatial resolution, provide structural and electronic information, and be applicable at both laboratory and mass-production scales. Raman spectroscopy fulfils all of above requirements. Through Raman spectroscopy, one can identify unwanted by-products, functional groups, structural damage and chemical modifications introduced during the preparation, processing or placement of various LMs. Here we review new

developments of Raman spectroscopy on the 2-D TMDs. We first introduce the lattice vibrations and phonon dispersion of 1L-, 2L- and bulk MX_2 (Section 2). Then, we discuss the fundamentals of Raman scattering and its selection rule (Section 3). We outline the non-resonant (Section 4) and resonant Raman (Section 5) spectroscopy in areas of TMDs. Raman spectroscopy of the 2-D TMDs modified by the external conditions such as strain, pressures, temperature and electric field are given in Section 6. We further demonstrate the potentials of shear and layer breathing modes in characterization of thickness of unknown ML TMDs and probing the the interface coupling of two-dimensional hybrids and heterostructures (Section 7). We hope that such a discussion will enable a better understanding of the recent progresses on the phonon and Raman scattering of 2-D TMD from 1L, ML to bulk material, and be helpful to design and perform decisive Raman experiments to employ the great potentials of Raman spectroscopy on the various LMs and their hybrids and heterostructures.

2 Lattice vibrations and Phonon dispersion of 1L-, 2L- and bulk 2H-MX_2

2.1 Lattice vibrations at Γ point and its symmetry classification

Lattice vibrations can be classified based on the irreducibles presentations of symmetry group of crystals.[55] The unit cell of bulk MX_2 consists of two X-M-X units with total 6 atoms, suggesting that there are 18 phonon modes (3 acoustic and 15 optical modes). Bulk MX_2 has D_{6h} point group. Thus, the lattice vibrations of bulk MX_2 at Γ can be expressed by the irreducible representations of D_{6h} as follows[56,57]: $\Gamma = A_{1g} + 2A_{2u} + 2B_{2g} + B_{1u} + E_{1g} + 2E_{1u} + 2E_{2g} + E_{2u}$, where one A_{2u} and one E_{1u} are acoustic modes, A_{1g}, E_{1g} and E_{2g} are Raman (R) active, another A_{2u} and E_{1u} are infrared (IR) active, B_{2g}, B_{1u} and E_{2u} are optical inactive (Silent). The modes denoted by letter "E" here are doubly degenerate in xy plane.

Due to the lack of translational symmetry (τ) along the z axis which is perpendicular to the basal xy plane, there is a reduction in symmetry in FL- TMDs (NL-MX_2),[58] here, N is an integer and refers to the layer number. Odd NL-MX_2 (ONL-MX_2) has D_{3h} point group because of the presence of the horizontal reflection plane (σ_h) that passes through the transition metal atom (M). Particularly, the unit cell of 1L-MX_2 is composed of 3 atoms with 9 normal vibrational modes at Γ point expressed by based on D_{3h}[25,57]: $\Gamma = 2A_2'' + A_1' + 2E' + E''$, where one A_2'' and one E' are acoustic modes, another A_2'' is IR active, A_1' and E'' are R active, and another E' is both R and IR active, as shown in Fig.2(a). The point group of even NL-MX_2 (ENL-MX_2) is D_{3d} due to the existence of inversion symmetry i. σ_h existed in ONL- and bulk MX_2 is not present in ENL-MX_2.[58] In particular for 2L-MX_2, its unit cell is composed
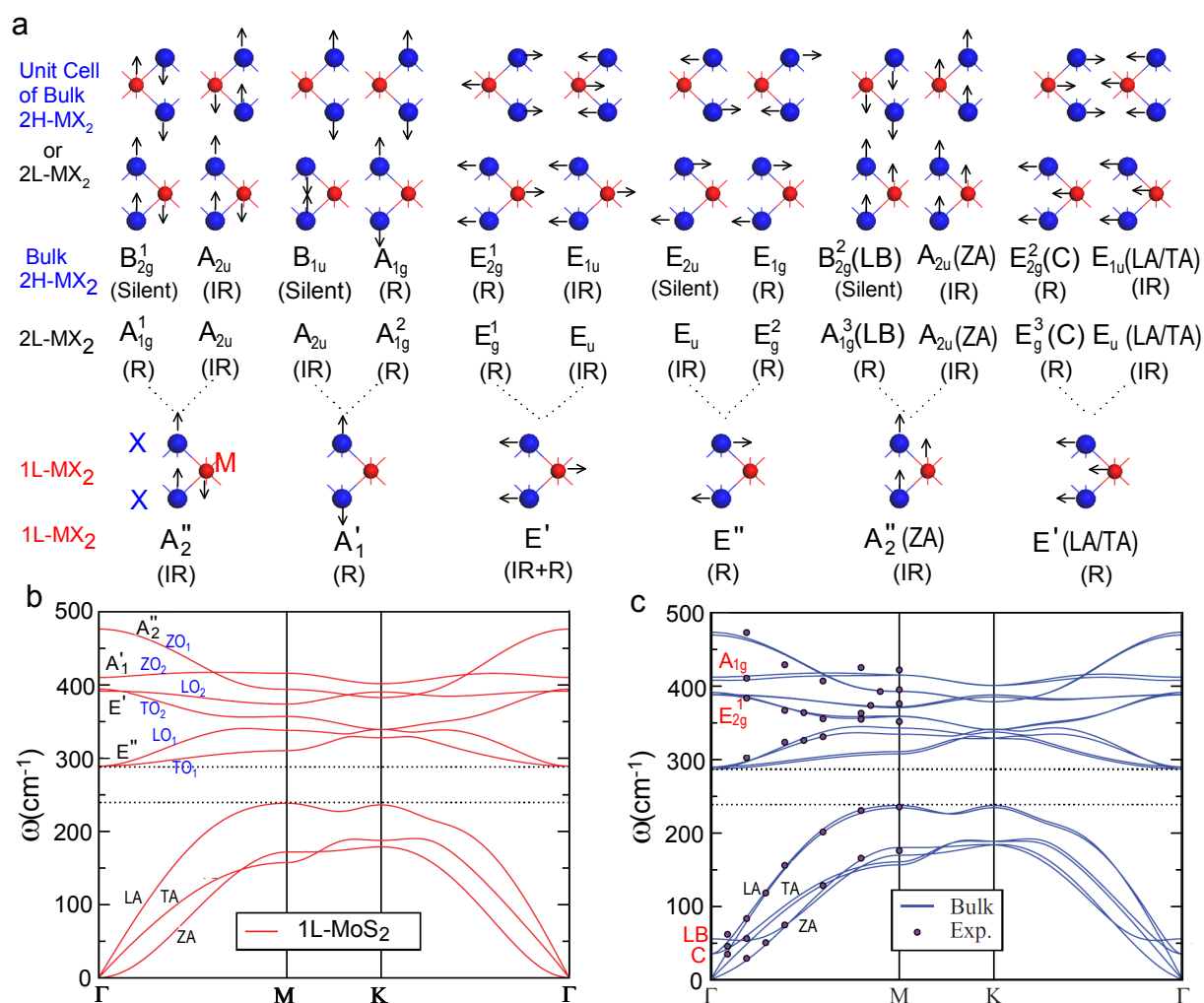
Fig. 2 (a) Symmetry and normal displacements of each optical vibration mode for bulk MX_2, 2L-MX_2 and 1L-MX_2. The Raman-active (R), infrared-active (IR), or both R and IR inactive (silent) modes are identified. The dotted lines demonstrate that each mode in 1L-MX_2 is split into two modes in both 2L-MX_2 and bulk MX_2 of which one vibrates in-phase and another out-of-phase. Phonon dispersion curves of (b) 1L-MX_2 and (c) bulk MX_2 are calculated for MoS_2. Points in (c) are experimental data extracted from neutron scattering measurents in ref.53. Reproduced with permission from ref.54. Copyright 2011, American Physical Society.

of 6 atoms belong to D_{3d}. There are 18 normal vibrational modes at Γ point[20,58]: $\Gamma = 3A_{1g}+3A_{2u}+3E_g+3E_u$, where one A_{2u} and one E_u are acoustic modes, the other A_{2u} and E_u are IR active, A_{1g} and E_g are R active, as demonstrated in Fig.2(a). It should be noted that the R and IR modes are mutually exclusive in MX_2 and ENL-MX_2 due to the presence of inversion symmetry i. The symmetry and normal mode displacement of each mode of bulk, 2L- and 1L- MX_2 are depicted in Fig.2(a). In general, 9N normal vibrational modes in NL-MX_2 at Γ point can be expressed based on its corresponding point group[20,58,59] as : $\Gamma_{ONL} = \frac{3N-1}{2}(A_1' + E'') + \frac{3N+1}{2}(A_2'' + E')$ for ONL-MX_2 (D_{3h}) and $\Gamma_{ENL} = \frac{3N}{2}(A_{1g} + E_g + A_{2u} + E_u)$ for ENL-MX_2 (D_{3d}). These 9N modes can be further clas-

sified into three categories according to their frequencies (will be discussed in Section 4): acoustic, ultra-low frequency and high frequency modes, as shown in Table.1, whose number of Raman active modes for the three categories are also included. Likewise, the symmetry classifications for lattice vibrations away from Γ point, e.g., at high-symmetry edges of the Brillouin zone, can also be obtained according to its corresponding point group, which has lower symmetry than that in Γ point.[55]

Each of 9 normal vibrational modes in 1L-MX_2 will split into the corresponding two modes in both 2L- and bulk MX_2, as shown in Fig.2(a) by dotted lines. For example, E' (R+IR) in 1L-MX_2 is split into E_g^1 (R) and E_u (IR) in 2L-MX_2, or E_{2g}^1

Table 1 Symmetry, Raman activity and number of acoustic, ultra-low frequency and high frequency modes in ENL-, ONL- and bulk MX_2. R, IR and S in brackets after symmetry refer to Raman active, infrared active and optically silent. All the "E" are doubly degenerated. Num(R) denotes the number of Raman active modes.

NL-MX_2	Acoustic	Ultra-low frequency		High frequency modes	Num(R)
		C modes	LBMs		
Bulk	$A_{2u}+E_{1u}$	$E_{2g}^2(R)$	$B_{2g}^2(S)$	$E_{1g}(R)+E_{1u}(IR)+E_{2g}(R)+E_{2u}(S)$ $+A_{1g}(R)+A_{2u}(IR)+B_{2g}(S)+B_{1u}(S)$	7
ENL	$A_{2u}+E_u$	$\frac{N}{2}E_g(R)+\frac{N-2}{2}E_u(IR)$	$\frac{N}{2}A_{1g}(R)+\frac{N-2}{2}A_{2u}(IR)$	$N(E_g(R)+E_u(IR)+A_{1g}(R)+A_{2u}(IR))$	9N/2
ONL	$A_2''+E'$	$\frac{N-1}{2}(E'(IR+R)+E''(R))$	$\frac{N-1}{2}(A_1'(R)+A_2''(IR))$	$N(E'(IR+R)+E''(R)+A_1'(R)+A_2''(IR))$	5(3N-1)/2

(R) and E_{1u} (IR) in bulk MX_2, where the displacements between the top and bottom layers are in phase for E_u/E_{1u}, but out of phase for E_g^1/E_{2g}^1. The positive integer in the upper right corner of mode notation "E" is used to distinguish the modes with same symmetry (e.g., E_{2g}^1 and E_{2g}^2 in Fig.2(a)), with general applicability to other modes. In the case of E_g^1/E_{2g}^1 in 2L-/bulk MX_2, additional "spring" coupling between X atoms of neighboring layers increases its frequency with respect to E_u/E_{1u}. This is known as "Davydov splitting",[60] which also happens to other modes in 2L- and bulk MX_2. Thus, the position of E_{2g}^2, Pos(E_{2g}^2), in bulk MX_2 is expected to be larger than Pos(E_{1u}). However, this is not the case in bulk MoS_2 where Pos(E_{2g}^2) is ~ 1 cm^{-1} lower than Pos(E_{1u}) due to the existence of other causes beyond the weak interlayer interaction.[61] Interesting splitting happens in acoustic A_2'' (ZA) and E' (LA/TA) in 1L-MX_2. A_2'' (ZA) in 1L-MX_2 will be split into A_{1g}^3 and A_{2u} (ZA) in 2L-MX_2, or B_{2g}^2 and A_{2u} (ZA) in bulk MX_2, while E' (LA/TA) in 1L-MX_2 splits into E_g^3 and E_u in 2L-MX_2, or E_{2g}^2 and E_{1u} (LA/TA) in bulk MX_2. A_{1g}^3/B_{2g}^2 and E_g^3/E_{2g}^2 in 2L-/bulk MX_2 are vividly referred as layer breathing (LB) and shear modes, which corresponds to the relative motions of its two X-M-X layers perpendicular and parallel to the layer plane, respectively. Similar shear mode has been observed in multilayer graphenes.[17] It is usually named as C because it provides a direct measurement of the interlayer coupling.[17]

2.2 Phonon dispersion

Away from Γ point, normal vibrational modes are dispersive with respect to wave vector q. The calculated phonon dispersions by density functional theory (DFT) within local density approximation (LDA) of 1L- and bulk MoS_2 are displayed in Figs.2(b) and 2(c).[54]

The phonon dispersion of 1L-MX_2 has three acoustic and six optical branches inheriting from the 9 vibrational modes at Γ point. The three acoustic branches include the in-plane longitudinal acoustic (LA) and transverse acoustic (TA) ones and the out-of-plane acoustic (ZA) one. The LA and TA branches have a linear dispersion and higher frequency than the ZA one around Γ.[54,62,63] The six optical branches are two in-plane longitudinal optical (LO$_1$ and LO$_2$), two in-plane transverse optical (TO$_1$ and TO$_2$) and two out-of-plane optical (ZO$_1$ and ZO$_2$) branches. These six optical modes at Γ point correspond to the irreducible representations as follows (Fig.2(b)): E'' (LO$_1$ and TO$_1$), E' (LO$_2$ and TO$_2$), A_2'' (ZO$_1$) and A_1' (ZO$_2$). Since MX_2 are slightly polar materials, certain IR-active phonon modes (for example, E') display LO-TO splitting due to the coupling of the lattice to the macroscopic electric field created by the relative displacements of M and X atoms in long-wavelength limit.[54,61,64] In addition, there is a bandgap between acoustic and optical branches, which is ~ 100 cm^{-1} for MoS_2 (Figs.2(b) and 2(c)) and WS_2, ~ 30 cm^{-1} for WSe_2 and ~ 15 cm^{-1} for $MoSe_2$ (See Electronic Supplementary Information (ESI)-Fig.S1).[54,62,63]

For 2L- and bulk MX_2, there are 18 phonon branches, which are split from 9 phonon branches in 1L-MX_2. Owing to the weak van der Waals interlayer interaction in 2L- and bulk MX_2, the frequency splitting of the corresponding two branches in 2L- and bulk MX_2 from each optical branch in 1L-MX_2 is very small, resulting in resemblance of optical phonon dispersion curves among 1L-, 2L- and bulk MX_2. For example, the phonon dispersions of 1L- (Fig.2(b)) and bulk (Fig.2(c)) MoS_2 are much similar, except three new branches below 100 cm^{-1} in bulk due to interlayer vibrations. The general features of 1L-, 2L- and bulk MoS_2[54], WS_2[54,65], WSe_2[63] and $MoSe_2$[66] are similar to each other. However, their phonon frequencies are much different. (See Fig.2(b) and ESI-Fig.S1) In comparison to 1L-MoS_2, the phonon bands in 1L-WS_2 are shifted down to lower frequencies, which is mainly due to the larger mass of W atoms.[54] Similar behaviors happen between 1L-WSe_2 and 1L-WS_2.[63,66] Furthermore, the interlayer phonons in bulk MX_2 are different from each other, which is

due to their intrinsic differences in both the whole mass of MX_2 and interlayer coupling strengths.

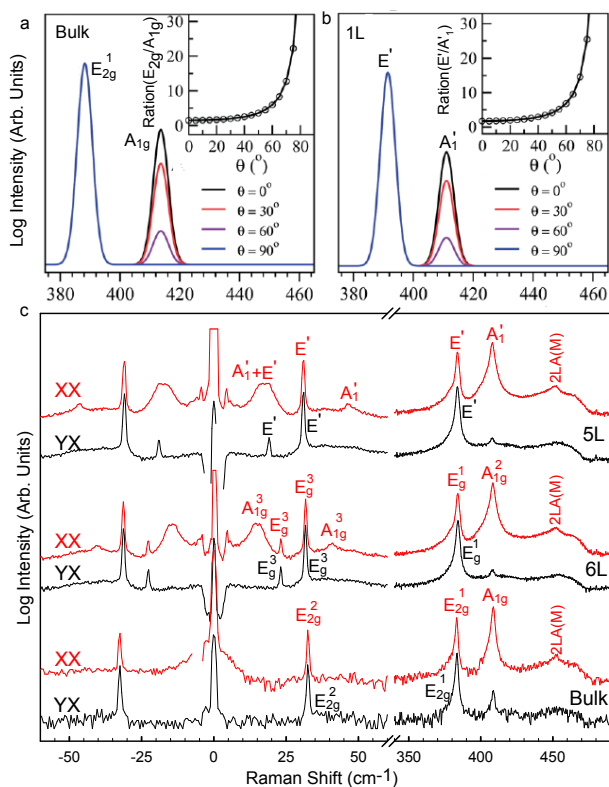# 3 Raman scattering and its selection rule of phonons in 1L-, FL- and bulk MX_2

Fig. 3 Calculated Raman spectra of (a) bulk and (b) 1L-MoS$_2$ with polarization vectors of $e_i(1, 0, 0)$ and e_s $(cos\theta, sin\theta, 0)$ for the incoming and scattered photons, respectively. The inset figures show I(E_{2g}^1)/I(A_{1g}) and I(E')/I(A'_1) as a function of θ. Reproduced with permission from ref.67. Copyright 2014, Royal Society of Chemistry. (c) Raman spectra of 5L-, 6L- and bulk MoS$_2$ measured under XX (red) and YX (black) polarization configurations. Here, XX and YX refer to $\theta = 0$ and $\theta = \pi/2$, respectively. The irreducible representation of each mode is indicated. Reproduced with permission from ref.19. Copyright 2013, American Physical Society.

Raman scattering is one of the main methods for obtaining information about the lattice vibration information of a crystal. In the Raman scattering process for a crystal, an incident photon from a laser can absorb or emit a phonon of the crystal, and is then scattered into surroundings in all directions. As a result, the photon loses (Stokes) or gains (anti-Stokes) the energy of the phonon, which is then detected and analyzed. Such Raman process is called as first-order Raman process. The process is called as second-order Raman process if involved with two phonons. Under the restriction of the momentum conservation, only the phonon with wavevector $q \approx 0$ (Γ point) can contribute to the first-order Raman scattering. The two phonons in second-order Raman process should have opposite wavevector q. The second-order Raman scattering is usually much weaker than the first-order one, but will be resonantly enhanced by the interband transition of a semiconductor. This enhancement makes it possible to detect the phonons at the edge of Brillouin zone (e.g., M and K points).[68] Furthermore, under the excitonic resonance condition, the symmetry of exciton levels could mediate the scattering of Raman-inactive phonon at Γ point.[69] Non-resonant and resonant Raman process in TMDs will be discussed in Section 4 and Section 5.

The Raman scattering intensity of a Raman-active mode in a crystal can be expressed by the defined Raman tensor (R) in the crystal as: $d\sigma/d\Omega = |e_s \cdot R \cdot e_i|^2$, here e_i and e_s are the polarization vectors of the incoming and scattered photons. The above equation results in the Raman selection rule of $R_{\mu,\nu} \neq 0$, here, $R_{\mu,\nu}$ is one component of R. Furthermore, $|e_s \cdot R \cdot e_i|^2$ establishes the selection rule for Raman spectrum of the Raman mode on e_i and e_s. R for a Raman mode with specific symmetry can be found in some standard references.[70,71]

For example, Raman active modes in Bulk MX_2 are denoted by A_{1g}, E_{1g} and $2E_{2g}$ (E_{2g}^1 and E_{2g}^2). Their R are listed as follows[70]:

$$A_{1g}: \begin{pmatrix} a & 0 & 0 \\ 0 & a & 0 \\ 0 & 0 & b \end{pmatrix},$$

$$E_{1g}: \begin{pmatrix} 0 & 0 & 0 \\ 0 & 0 & c \\ 0 & c & 0 \end{pmatrix}, \begin{pmatrix} 0 & 0 & -c \\ 0 & 0 & 0 \\ -c & 0 & 0 \end{pmatrix},$$

$$E_{2g}: \begin{pmatrix} 0 & d & 0 \\ d & 0 & 0 \\ 0 & 0 & 0 \end{pmatrix}, \begin{pmatrix} d & 0 & 0 \\ 0 & -d & 0 \\ 0 & 0 & 0 \end{pmatrix}.$$

Under the back-scattering configuration, e_i and e_s are within xy plane, which can be set to, $e_i = (cos\theta, sin\theta, 0)$ and $e_s = (1, 0, 0)$, respectively, where θ is the angle between e_i and e_s. Usually, $(1,0,0)$, $(0,1,0)$ and $(0,0,1)$ of e_i and e_s are, respectively, denoted as X, Y and Z. Thus, the intensity of A_{1g} modes, I(A_{1g}), in Bulk MX_2 is proportional to $a^2 cos^2\theta$, which monotonically reduces from maximum to minimum with θ being varied from 0 (XX) to $\pi/2$(YX). E_{1g} is double-degenerated and there are two Raman tensors, R_x and R_y. I(E_{1g})=$|e_s \cdot R_x \cdot e_i|^2 + |e_s \cdot R_y \cdot e_i|^2 = 0$, which means that it can not be detected under this polarization configuration. Similarly, I(E_{2g})=d^2, independent on θ. The calculated Raman spectra of bulk MoS$_2$ in Fig.3(a) show a decrease of $I_{A_{1g}}$ and a constant of $I_{E_{2g}}$ for θ varying from from 0 to $\pi/2$.[67]

For Raman active A_{1g} and E_g in ENL-MX$_2$, their R are listed as follows:

$$A_{1g}: \begin{pmatrix} a & 0 & 0 \\ 0 & a & 0 \\ 0 & 0 & b \end{pmatrix},$$

$$E_g: \begin{pmatrix} c & 0 & 0 \\ 0 & -c & d \\ 0 & d & 0 \end{pmatrix} \begin{pmatrix} 0 & -c & -d \\ -c & 0 & 0 \\ -d & 0 & 0 \end{pmatrix}.$$

A_{1g} in ENL-MX$_2$ has an identical R to that in bulk MX$_2$, indicating similar polarization properties as discussed above, i.e., A_{1g} is absent under YX configuration and approaches to maximum intensity under XX configuration. However, E_g is present under both XX and YX configurations.

R of Raman active A_1', E'' and E' in ONL-MX$_2$ are listed as follows:

$$A_1': \begin{pmatrix} a & 0 & 0 \\ 0 & a & 0 \\ 0 & 0 & b \end{pmatrix},$$

$$E': \begin{pmatrix} 0 & d & 0 \\ d & 0 & 0 \\ 0 & 0 & 0 \end{pmatrix} \begin{pmatrix} d & 0 & 0 \\ 0 & -d & 0 \\ 0 & 0 & 0 \end{pmatrix},$$

$$E'': \begin{pmatrix} 0 & 0 & 0 \\ 0 & 0 & c \\ 0 & c & 0 \end{pmatrix} \begin{pmatrix} 0 & 0 & -c \\ 0 & 0 & 0 \\ -c & 0 & 0 \end{pmatrix}.$$

In fact, R of A_1', E'' and E' is, respectively, identical to that of A_{1g}, E_{1g} and E_{2g}. It results from the correlation between D_{3h} and D_{6h}.[55] Thus, these modes show similar polarization dependence to their corresponding modes in bulk MX$_2$, as shown in Fig.3(b) for 1L-MoS$_2$.

Based on the above discussion, we can assign all the observed Raman modes in ONL- and ENL-MX$_2$. As an example, Raman spectra of 5L-, 6L- and bulk MoS$_2$ under XX and YX configurations are depicted in Fig.3(c). Those modes which only appear under XX but not YX configurations correspond to the relative motions of the atoms perpendicular to the layer plane, and are assigned by A_1' (ONL) and A_{1g} (ENL and bulk), while those exist under both XX and YX correspond to the relative motions of the atoms within xy plane, and are assigned as E' (ONL), E_g (ENL) and E_{2g} (bulk). The upper right corner of mode notation in Fig.3(c) is used to distinguish the modes with same symmetry. Furthermore, polarized Raman measurement can distinguish two overlapped modes in the unpolarized Raman spectrum by their different polarization dependence. For example, in 5L-MoS$_2$, the mode at 19 cm^{-1} (E') can be identified under YX although it is overlapped under XX due to the presence of the broad A_1' at 17 cm^{-1}. The properties of these modes including the 2LA(M) mode at $\sim$ 450 cm^{-1} will be discussed latter.

4 Non-resonant Raman scattering in TMDs

4.1 Anomalous frequency trends of E_{2g}^1 and A_{1g} with increasing layer number

From Table.1, there are seven Raman active modes (A_{1g}, doubly degenerate $2E_{2g}$ and doubly degenerate E_{1g}) for bulk MX$_2$. Under back-scattering Raman configuration, E_{1g} is absent according to its Raman tensor. Thus, three Raman peaks are expected in the Raman spectrum. Indeed, three peaks, $\sim$ 33.5 (E_{2g}^2), $\sim$ 383.6 (E_{2g}^1) and $\sim$ 408.7cm^{-1} (A_{1g}), are detected in bulk MoS$_2$ and assigned by their polarization properties, as shown in Fig.3(c). The frequency of the corresponding modes in 1L- and ML-MX$_2$ is expected to be dependent on the layer number in frequency. Based on the discussions in Section 2, the denotations of these modes in ONL- (E' and A_1') and ENL- (E_g and A_{1g}) MX$_2$ are different to bulk due to their intrinsic different symmetries. When we discuss the evolution of peak parameters of Raman modes from bulk to monolayer, for the sake of convenience, we simply refer the corresponding modes as E_{2g}^1 and A_{1g} in bulk for the high-frequency modes as commonly done in the literature.[18,54]

The layer number (N) dependence of peak position and width for E_{2g}^1 and A_{1g} of NL-MoS$_2$ is depicted in Fig.4(a). Pos(E_{2g}^1) and Pos(A_{1g}) show opposite trends from bulk to 1L, as summarized in Fig.4(b). However, based on the linear chain model (only van der Waals interaction is included), the two modes would decrease in frequency from 2L to 1L.[19] This unexpected trend of E_{2g}^1 indicates that other interactions beyond van der Waals forces exist,[18,54,73] which is also revealed by the anomalous Davydov splitting between E_{2g}^1 and E_{1u} (Section 2). Molina-Sánchez and Wirtz carefully examined the self-interaction term of S atoms for A_{1g} (Mo atoms stay still) and both S and Mo atoms for E_{2g}^1 in 1L- and bulk MoS$_2$.[54] They attributed the unexpected trends of Pos(E_{2g}^1) to the long-range Coulomb term, which decreases considerably in few layer and bulk due to the significant increase of the dielectric tensor with N.[54] The long-rang Coulomb interaction is induced by the effective charges resulting from the relative displacement between Mo and S atoms. E_{1g} (Fig.2(a), observable under XZ and YZ polarization configuration) also shows relative displacement, thus, is expected to present anomalous frequency trend.[54]

Similar anomalous frequency trends with N between A_{1g} and E_{2g}^1 exist in NL- WS$_2$, WSe$_2$ and MoSe$_2$. Figs.4(c) and (d) show the trends for NL-WS$_2$.[72] Those in WSe$_2$ and MoSe$_2$ are depicted in ESI-Fig.S2.[72,74] The trends favor the layer number identification of MX$_2$ through their relative frequency difference.[18,75] For example, the frequency difference $\Delta\omega(A_{1g} - E_{2g}^1)$ of NL-MoS$_2$ (N=1-5) can be expressed as $\Delta\omega(A_{1g} - E_{2g}^1) = 25.8 - 8.4/N$, as shown in Fig.4(b). How-
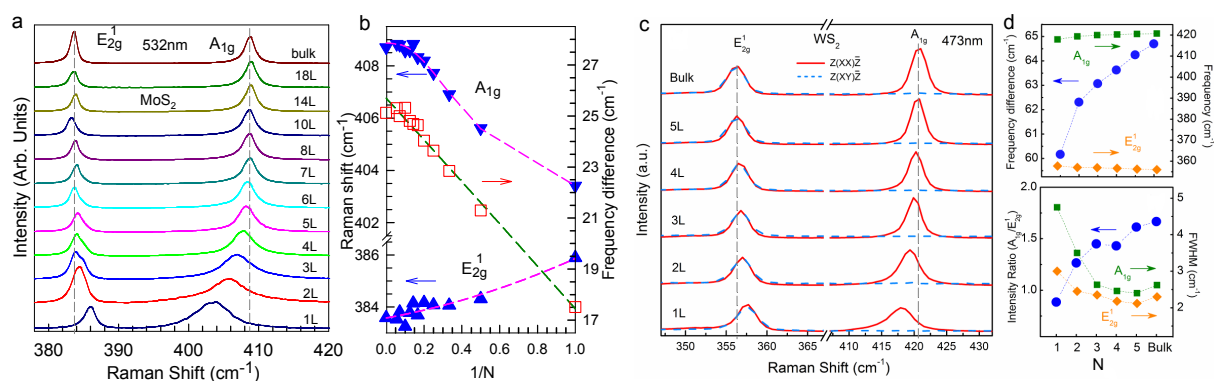
Fig. 4 (a) Raman spectra of NL- (N=1-8, 10, 14, 18) and bulk MoS$_2$. Two grey-dashed lines indicate Pos(E_{2g}^1) and Pos(A_{1g}) in bulk MoS$_2$. (b) Frequency (ω) and its discrepancy ($\Delta\omega$) between E_{2g}^1 and A_{1g} as a function of 1/N. For $1 \leq N \leq 5$, the linear fitting gives $\Delta\omega(A - E) = 25.8 - 8.4/N$. (c) Polarized Raman spectra of 1-5L and bulk WS$_2$ with their frequency, frequency discrepancy, I(A_{1g})/I(E_{2g}^1) and peak width summarized in (d). Reproduced with permission from ref.72. Copyright 2013, Royal Society of Chemistry.

ever, further N identification for $N > 5$ must be done by other methods, such as interlayer vibration modes to be discussed in following subsection. This empirical expression only accounts for exfoliated NL-MoS$_2$, but not for NL-MoS$_2$ grown by CVD. Actually, $\Delta\omega(A_{1g} - E_{2g}^1)$ for CVD-grown 1L-MoS$_2$ is ~ 20 cm^{-1}, ~ 2 cm^{-1} larger than that in exfoliated 1L-MoS$_2$.[76]

4.2 Interlayer shear and layer breathing modes

Since the restoring forces for A_{1g}^3/B_{2g}^2 (LB) and E_g^3/E_{2g}^2 (C) in ML- and bulk MX$_2$ are weak due to their van der Waals interlayer interactions, the modes are expected to have low frequencies. Indeed, the C mode of bulk MoS$_2$ is located at 33.5 cm^{-1}, as seen in Fig.3(c). The LB mode is absent in the Raman spectrum of bulk MX$_2$ since it is Raman inactive. No C or LB modes are expected in 1L-MX$_2$ because there is only one X-M-X layer. However, when 1L-MX$_2$ is vertically stacked to form ML-MX$_2$, a series of C and LB modes appear at ultra-low-frequency (ULF) region, whose frequencies will significantly depend on the weak interlayer restoring force and layer number N.

Typical frequencies of LB modes are usually under ~ 100 cm^{-1}, while those of C modes are smaller, bellow ~ 50 cm^{-1}. The traditional approach to perform very low-frequency Raman measurements involves the use of a triple spectrometer, which has been applied to ML- MoS$_2$ or WSe$_2$ by several groups.[19,20,77–79] A cross-polarized backscattering geometry can be used to suppress the Rayleigh signal to obtain Raman spectra very close to the laser line.[77] Because the spectral throughput is very low for the triple spectrometer, the system is difficult to be applied to various MX$_2$ and other 2-D materials. For example, there is no report on the C modes in ML graphenes by the triple spectrometer up to now. Tan

et al. by combining a single monochromator with BragGrate bandpass and notch filters (OptiGrate Corp.) can detect ULF Raman signal down to ~ 5 cm^{-1} with high signal throughput. They had successfully observed C and LB modes for ML graphenes.[17,80,81] This ULF technique has been applied to multilayer MoS$_2$ up to 18L, where several sets of C and LB modes were detected, as shown in Fig.5(a).[19] Similar results are also revealed in multilayer WSe$_2$ up to 7L.[20](ESI-Fig.S3) Figs.5(b) and (c) show frequency and FWHM of typical C and LB modes as a function of N. The larger FWHM of LBM in comparison to the C mode has been interpreted as its anharmonic feature with a significant enhancement of phonon-phonon scattering when N decreases.[79]

In order to elucidate the origin of these C and LB modes in NL-MX$_2$, a diatomic chain model (DCM) can be built (see Fig.5(d)), where only two force constants are needed to describe the vibrations under nearest-neighbor interlayer interaction approximation: α_{XX} and α_{XM}, where α_{XX} is the force constant per unit area between two nearest X planes in two adjacent layers, and α_{XM} is force constant per unit area between the nearest X and M planes within a MX$_2$ layer. Their $\perp$ (or $\parallel$) components are used to describe the vibrations along z axis (or with xy plane). By solving the dynamic eigen-equation and fitting the results to observed E'/A_1' in 1L-MX$_2$ and C/LB modes in NL-MX$_2$ (N>2), one can obtain the strength of intra-/interlayer coupling and the atomic displacements. In MoS$_2$, we have $\alpha_{SS}^\perp/\alpha_{SMo}^\perp$=2.6%, and $\alpha_{SS}^\parallel/\alpha_{SMo}^\parallel$=1.5%. The atomic displacements of both C and LB modes in 3L- MoS$_2$ are depicted in Fig.5(e), where corresponding irreducible representations are determined by symmetry analysis on these displacements. In NL-MX$_2$, there are $(N - 1)$ LB modes and $(N - 1)$ doubly degenerate C modes from symmetry analysis (Table.1). When N is odd, there are $\frac{N-1}{2} E'$ and $\frac{N-1}{2} E''$ for C modes, and $\frac{N-1}{2}$
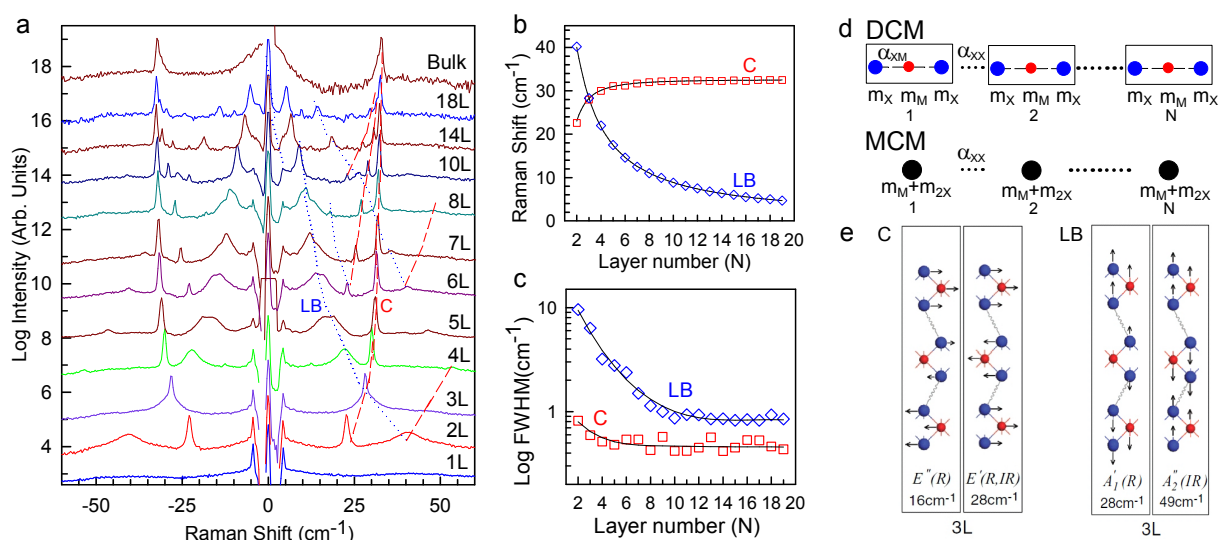
Fig. 5 (a) Stokes and anti-Stokes Raman spectra of NL-(N=1-8, 10, 14, 18) and bulk MoS$_2$ between -60 and 60 cm^{-1}. Dashed and dotted lines are guides to the eye for the frequency trends of C and LB modes. (b) Frequency and (c) FWHM of C and LB modes as a function of N. Solid lines are guides to the eye. Reproduced with permission from ref.19. Copyright 2013, American Physical Society. (d) Diatomic chain model (DCM) and monatomic chain model (MCM) for NL-MX$_2$, here, α_{XX} and α_{XM} describe the force constant between X-X layers and X-M layers, respectively. m$_X$ and m$_M$ are mass of the X and M layers, respectively. (e) Symmetry, frequencies and atomic displacements for C and LB modes in 3L-MoS$_2$, which are Raman-active (R) and/or infrared-active (IR).

$A_1^{'}$ and $\frac{N-1}{2} A_2^{''}$ for LB modes. When N is even, there are $\frac{N}{2}$ E_g and $\frac{N-2}{2} E_u$ for C modes, and $\frac{N}{2} A_{1g}$ and $\frac{N-2}{2} A_{2u}$ for LB modes. The peak positions of all C and LB modes in NL-MX$_2$ can be calculated based on DCM. Those of 5L-, 6L- and bulk MoS$_2$ are summarized in Table.2 along with the experimental data (Fig.3(c)) and polarization properties.

Based on DCM, the relative displacements between Mo and two S atoms in an S-Mo-S layer for all the C and LB modes in ML-MoS$_2$ are very small. As an example, the relative displacement in 2L-MoS$_2$ is around 0.6%, which further decreases with increasing N. Thus, a monatomic chain model (MCM) can be considered if one treats an entire X-M-X layer as a single ball, as depicted in Fig.5(d). Taking the entire layer as a ball with mass $(M = m_M + 2m_X)$ and interlayer coupling $\alpha_{XX}^{\perp}$ for LB modes, and $\alpha_{XX}^{\parallel}$ for C modes, the eigen-equation can be analytically solved and the relation between position and N for both C and LB modes can be obtained, $\omega_{C,2N_0}^{\pm}(N) = \omega_C(2)\sqrt{1 \pm cos(N_0\pi/N)}$ and $\omega_{LB,2N_0}^{\pm}(N) = \omega_{LB}(2)\sqrt{1 \pm cos(N_0\pi/N)}$ (N and N$_0$ are integer and $N \geq 2N_0$), where $\omega_C(2)$ and $\omega_{LB}(2)$ refer the frequencies of C and LB modes in 2L-MX$_2$, respectively. These vibration modes can be assigned to a series of branches, as shown in Fig.6 for NL-MoS$_2$. Each branch of the C ($\omega_{C,2N_0}^{\pm}(N)$, denoted as C$_{2N_0}^{\pm}$) and LB ($\omega_{LB,2N_0}^{\pm}(N)$, denoted as LB$_{2N_0}^{\pm}$) modes includes one high-frequency subbranch ("+") and one low-frequency subbranch ("−"). The two subbranches cross at

N=2N$_0$. In the case of bulk (N = ∞), we have $\omega_C^{+}(bulk) = \sqrt{2}\omega_C(2)$ and $\omega_{LB}^{+}(bulk) = \sqrt{2}\omega_{LB}(2)$. Thus, the frequencies of C and LB modes in bulk can be obtained from those detected in 2L-MX$_2$. The theoretical results from the DCM and MCM are in good agreement with the experimental data for NL-MoS$_2$, as shown in Fig.6. Once $\omega_C(2)$ and $\omega_{LB}(2)$ are obtained, the whole sets of relation between peak position and N for both C and LB modes are completely determined.

Because $\omega_C(2)$ and $\omega_{LB}(2)$ are, respectively, linked with force constants between two nearest S planes in adjacent layers: $\omega_C(2) = (1/\sqrt{2}\pi c)\sqrt{\alpha_{ss}^{\parallel}/M}$ and $\omega_{LB}(2) = (1/\sqrt{2}\pi c)\sqrt{\alpha_{ss}^{\perp}/M}$, the good agreement between MCM and experimental data for NL-MoS$_2$ is indicative of constant interlayer interaction from 2L, ML to bulk MoS$_2$.[19] Other TMDs show similar structures to MoS$_2$, which indicates the above equation can also be applied to these materials by replacing the $\omega_{LB}(2)$ and $\omega_C(2)$ with the corresponding values in other 2L-TMDs. Further, this MCM can predict the dependencies of C and LB modes on layer thickness in other LMs beyond TMDs, such as hBN.[19] It is also noted that C and LB modes are directly related to interlayer coupling, which has potential in probe of the interface coupling in folded (or twisted) TMDs and heterostructure built from TMDs.

Table 2 Symmetry, polarization (polar.), experimental positions (Exp., in cm^{-1}) and theoretical frequencies (Theo., in cm^{-1}) of all the C and LB modes in 5L-, 6L- and bulk MoS_2. The polarization configuration in the bracket is not available under the back-scattering condition.

		C		LB	
5L	mode	$E'(R,IR)$	$E''(R)$	$A_1'(R)$	$A_2''(IR)$
	polar.	XX,YX	(XZ,YZ)	XX	-
	Exp.	19.0, 31.1	-	17.5, 46.0	-
	Theo.	19.1, 31.0	-	17.5, 46.1	-
6L	mode	$E_g(R)$	$E_u(IR)$	$A_{1g}(R)$	$A_{2u}(IR)$
	polar.	XX,YX,(XZ,YZ)	-	XX	-
	Exp.	22.7, 31.2	-	14.6, 40.3	-
	Theo.	23.0, 31.5	-	14.6, 40.2	-
Bulk	mode	$E_{2g}^2(R)$		$B_{2g}^2(S)$	
	polar.	XX,YX		-	
	Exp.	33.5		-	
	Theo.	33.5		-	

4.3 Phonon dispersive trends away from Γ point

Due to the Heisenberg uncertainty principle, the fundamental $q \sim 0$ Raman selection rule is relaxed for a finite-size domain, allowing the participation of phonons away from the Brillouin-zone center (Γ). The phonon uncertainty goes roughly as $\Delta q \sim 1/d$, where d is the size of crystal domain. The Raman spectrum of 1L-MX_2 with small domain size could provide enough information on the phonon dispersion near Γ point. This usually gives a downshift and asymmetric broadening of the Raman peak. The corresponding Raman mode will usually red-shift in frequency.[82,83] The ion-implantation technique has been widely used to get nanocrystalline from graphene, ML graphenes and graphite.[84,85] Recently, smaller crystal size of 1L-MoS_2 and 1L-WS_2 is obtained by increasing the dosage of ion-implantations.[86] As shown in Figs.7(c) and 7(d), with increasing the ion-implantation dosage, the softening of E' and hardening of A_1' in 1L-MoS_2 were observed, while both E' and A_1' modes are soften in 1L-WS_2. Correspondingly, the ion-implantation also results in the reduction of PL intensity from A exciton. PL is almost quenched when the ion-implantation dosage is larger than 5×10^{13} Ar^+/cm^2, which indicates that 1L-MoS_2 is highly disordered.

To understand the above results, a phenomenological phonon confinement model originally proposed by Richer, Wang and Ley (WRL model)[87] has been applied to nanocrystalline of 1L-MoS_2 and 1L-WS_2 induced by ion-implantation. This model explained the frequency shifts of A_1' and E' of 1L-MoS_2 with increasing ion-implantation dosage, as shown in Fig.7(c) by vertical dash-dotted lines. The small hardening of A_1' in 1L-MoS_2 manifests that ZO_2 phonon branch increases in frequency slowly with q away from Γ point, which agrees with

the trend of ZO_2 dispersion in Fig.7(a). Similarly, the larger softening of E' in 1L-MoS_2 suggests that LO_2/TO_2 branches decrease rapidly with q away from Γ point. However, for the nanocrystalline 1L-WS_2, both A_1' and E' are softened with increasing ion-implantation dosage (Fig.7(d)), which can be well reproduced by the WRL model. When the ion dosage increases, the trend of phonon dispersion away from Γ point is steeper, the peak frequency shift is larger, and the peak profile is more asymmetric and broadening. Although LO_2 of 1L-WS_2 increase rapidly near M point (Fig.7(b)), only non-zero q close to Γ point can participate in the Raman process so that the corresponding blueshift of E' can not be observed.

4.4 Raman characterization of TMD alloys

Alloying materials with different band gaps have been widely used in the band gap engineering of bulk semiconductors. The realization of band gap tuning in atomically thin 2-D alloys and various choices of layered TMDs could allow wide range band gap tuning for applications of 2-D materials in nano-electronics and optoelectronics. Alloying monolayer TMD has been proposed by theoretical calculations[89,90] and demonstrated in experiments[91,92]. A series of monolayer TMD alloys ($Mo_{1-x}W_xS_2$, $x = 0$ to 1) have been cleaved from their bulk crystals.[91] Monolayer alloy film of $MoS_{2(1-x)}Se_{2x}$ of arbitrary composition can be grown by CVD through control of the S/Se ratio of the organic precursors used in the growth process.[92]

Structure characterization of 2-D alloys, such as composition and atom mixing, is of fundamental importance to their applications. Raman spectroscopy is a powerful tool to characterize structures of 2-D alloys by the frequency shift for alloy composition and by peak broadening for al-
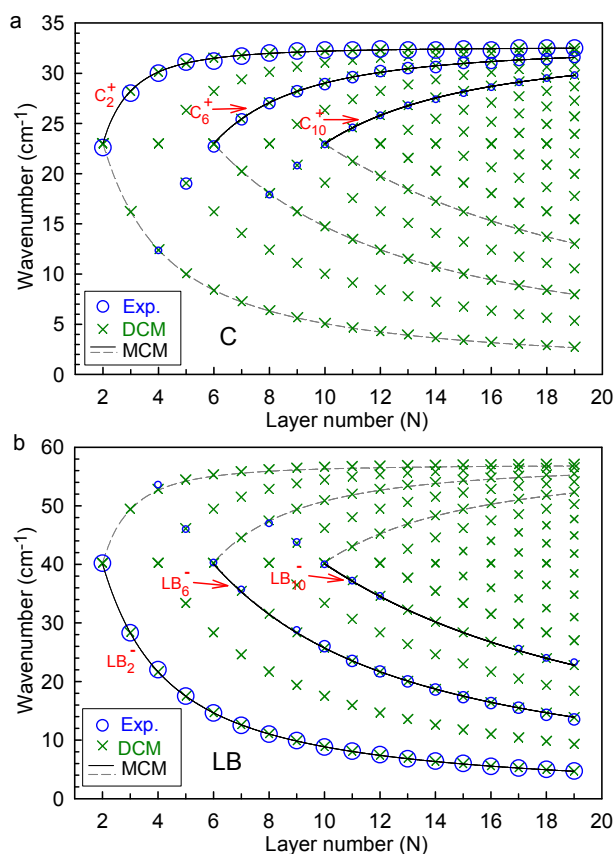
Fig. 6 Positions of (a) C and (b) LB modes of NL-MoS$_2$ as a function of N. The experimental data are shown by blue open circles whose diameter represents the Raman intensity of each mode. The green crosses are calculations from DCM. The gray dashed lines are another set of the C and LB modes based on the MCM. The black solid lines in (a) and (b) are, respectively, fitted by

$$\omega(N) = \omega(2)\sqrt{1+cos(N_0\pi/N)} \ (N{\geq}2N_0) \text{ and}$$
$$\omega(N) = \omega(2)\sqrt{1-cos(N_0\pi/N)} \ (N{\geq}2N_0)$$

for the phonon branches originating from 2L-(N_0=1), 6L-(N_0=3) and 10L-(N_0=5) MoS$_2$ based on MCM. They are simply denoted as C$^+_{2N_0}$ and LB$^-_{2N_0}$, respectively. Reproduced with permission from ref.19. Copyright 2013, American Physical Society.

Fig. 7 Phonon dispersions of ZO$_2$ ($A^{'}_1$ at Γ), LO$_2$ ($E^{'}$ at Γ) and TO$_2$ ($E^{'}$ at Γ) along Γ-M are depicted for (a) 1L-MoS$_2$ and (b) 1L-WS$_2$. The experimental (crosses) and calculated (solid lines) results of (c) 1L-MoS$_2$ and (d) 1L-WS$_2$ for different ion implantation doses. The dashed lines are the contribution of sub peaks from LO$_2$ and TO$_2$ branches. The spectra are normalized to $A^{'}_1$.

Fig. 8 (a) Raman spectra of Mo$_{1-x}$W$_x$S$_2$ monolayers with different W composition x. The three solid lines as guides to the eye show Pos($E^{'}$) and Pos($A^{'}_1$) peaks with W composition x. (b) Composition-dependent Raman frequencies of each mode in Mo$_{1-x}$W$_x$S$_2$ monolayers. Reproduced with permission from ref.88. Copyright 2014, Royal Society of Chemistry.

loy degree.[93] In comparison to FL and bulk Mo$_{1-x}$W$_x$S$_2$, Mo$_{1-x}$W$_x$S$_2$ monolayer shows smaller frequency difference between $A^{'}_1$ and $E^{'}$ and similar polarization dependence of Raman modes.[91] Composition-dependent unpolarized Raman spectra of Mo$_{1-x}$W$_x$S$_2$ monolayer with W composition from 0 to 1 is shown in Fig.8(a). The assignments of $A^{'}_1$ and $E^{'}$ are based on the polarized Raman spectra.[19] Similar to that of Mo$_{1-x}$W$_x$S$_2$ bulk alloys[94], $A^{'}_1$ and $E^{'}$ show one-mode and two-mode behaviors, respectively. As shown in Fig.8(b), with W composition x increases from 0 to 1, $A^{'}_1$ mode continuously upshifts, while MoS$_2$-like $E^{'}$ mode shifts to lower frequency. WS$_2$-like $E^{'}$ appears at $x = 0.2$ and moves slowly towards
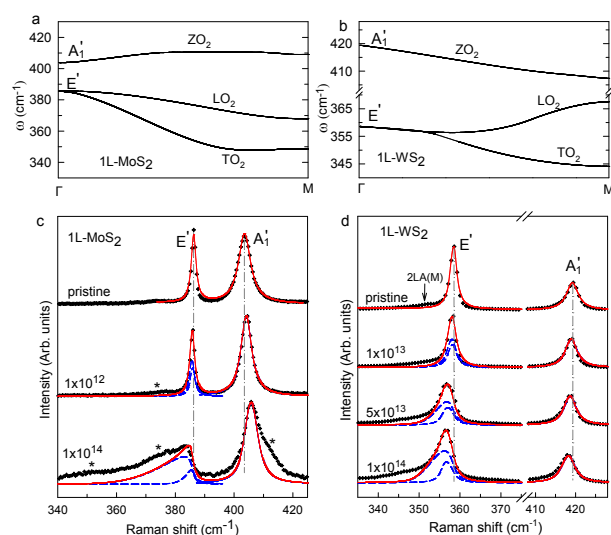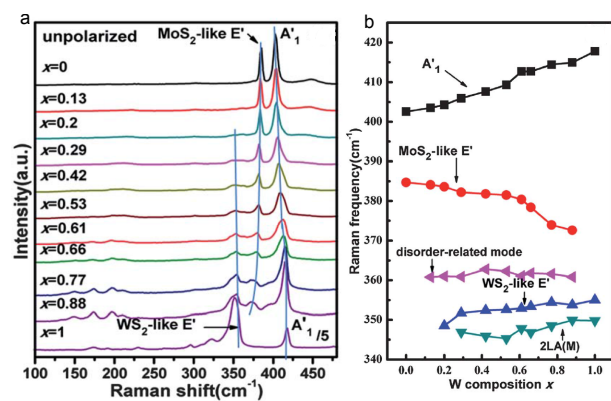
higher frequency. As W composition increases, the relative intensity of WS$_2$-like $E^{'}$ increases, while that of MoS$_2$-like $E^{'}$ decreases. The Raman peak at ~ 360 cm^{-1} appearing from $x = 0.13$ to $x = 0.77$ was assigned to an alloy disorder-related peak, which is not sensitive to the alloy composition. The peak frequency at ~ 346 cm^{-1} is attributed to 2LA(M) of WS$_2$ and overall shows a decrease trend with decreasing W composition (Fig.8(b)). Based on the modified random-

element-isodisplacement model, Chen *et al.* reproduced the dependence of $A_1^{'}$, MoS$_2$-like $E^{'}$ and WS$_2$-like $E^{'}$ on W composition x, which can be used to quantify Mo/W compositions.[88,95] This systematic Raman scattering investigation on Mo$_{1-x}$W$_x$S$_2$ monolayer is very helpful for the spectroscopic determination of composition and alloy degree for various 2-D crystal alloys.

5 Resonant Raman scattering in TMDs

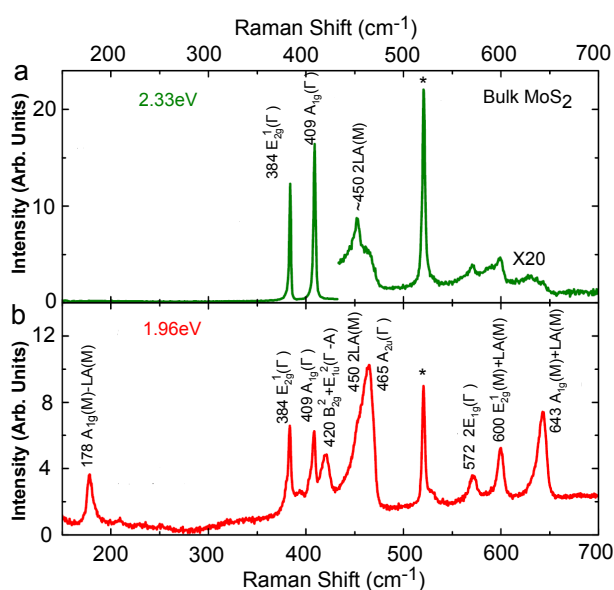## 5.1 Phonons of bulk MX$_2$ at Γ and M points

Fig. 9 (a) Non-resonant and (b) resonant Raman spectra of bulk MoS$_2$ at room temperature. The peak position and corresponding assignment of each mode are presented, where Γ, M and Γ-A in the bracket after each mode represent involved phonons which come from Γ, M points and along Γ-A direction. The star (*) labels the Raman peak of Si ~ 520 cm^{-1}. Reproduced with permission from ref.96. Copyright 2014, AIP Publishing LLC.

At first, we will check the non-resonant and resonant Raman spectra of bulk MoS$_2$,[96] as depicted in Fig.9. The non-resonant and resonant Raman spectra of bulk WS$_2$ and WSe$_2$ are afforded in ESI-Fig.S4. The non-resonant spectrum is usually dominated by four basic vibration modes lying at Γ point[18,19,56,57]: E_{2g}^2 (32 cm^{-1}, C), E_{1g} (286 cm^{-1}), E_{2g}^1 (384 cm^{-1}) and A_{1g} (409 cm^{-1}). Because E_{1g} (286 cm^{-1}) is forbidden under backscattering geometry according to its Raman tensor, it does not appear in the spectrum excited by 2.33 eV in Fig.9(a). A very weak peak ~ 450 cm^{-1} (2LA(M)) and several weaker peaks above 520 cm^{-1} are also observed in the non-resonant Raman spectrum in Fig.9(a).
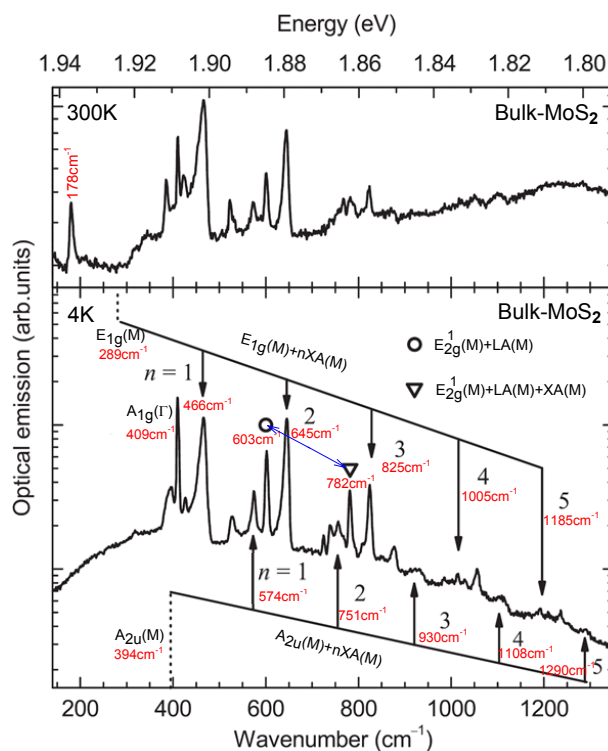

Fig. 10 Resonant Raman spectra of bulk MoS$_2$ at room temperature (top) and at low temperature of 4.2 K (bottom). The black arrows denote the five phonon replica of E_{1g}(M) and A_{2u}(M). The mode at 782 cm^{-1} is the first phonon replica of the mode at 603 cm^{-1}, as indicated by blue line with double arrows. Reproduced with permission from ref.96. Copyright 2014, AIP Publishing LLC.

Because 1.96 eV is close to the energy (~ 1.88 eV at room temperature) of A exciton in bulk MoS$_2$,[8] it is usually used to excite the resonant Raman spectrum of bulk MoS$_2$, as shown in Fig.9(b).[96] Under the resonant excitation, more intense modes are found at and usually assigned as:[69,97,98] ~ 178 cm^{-1} (A_{1g}(M)-LA(M)), ~ 420 cm^{-1} ($B_{2g}^2 + E_{1u}^2$ (Γ-A)), ~ 465 cm^{-1} (2LA(M)(~ 450 cm^{-1}) and A_{2u}(Γ) (~ 465 cm^{-1})), ~ 572 cm^{-1} (2E_{1g}(Γ)), ~ 600 cm^{-1} (E_{2g}^1(M)+LA(M)) and ~ 643 cm^{-1} (A_{1g}(M)+LA(M)). The mode ~ 420 cm^{-1} is highly dispersive and explained by Sekine *et al.* as a second-order Raman process, where a polariton created by incident laser in photon-like branch will first be scattered by emitting a longitudinal dispersive quasi-acoustic (QA) phonon along Γ-A, then scattered by emitting a E_{1u}^2 phonon (which is dispersionless along Γ-A) into the exciton-like final state.[98] Here, Γ-A is perpendicular to the 2-D Brillouin plane. The QA phonon at the Γ point is the B_{2g}^2 of MoS$_2$. The energy difference of its Stokes and anti-Stokes under 217K is ~ 4.7 cm^{-1}.[99] Pos(B_{2g}^2) can be deduced from the dispersive $B_{2g}^2 + E_{1u}^2$(Γ-A) based on the exciton-polariton dispersion.[98] The most intense

and asymmetric resonant mode lying ~ 465 cm^{-1} was first assigned by Stacy et al.[100] as $2LA$(M), then suggested by Frey et al. to be composed of double-mode feature, second-order $2LA$(M) and first-order $A_{2u}(\Gamma)$, due to its splitting in nanoparticles.[69] The mode ~ 643 cm^{-1} is assigned as A_{1g}(M)+LA(M), which can be used to estimate the energies of A_{1g}(M) and LA(M) when combined with ~ 178 cm^{-1} (A_{1g}(M)-LA(M)). A_{1g}(M) and LA(M) are found ~ 410.5 cm^{-1} and ~ 232.5 cm^{-1}, respectively.[96] The frequency (~ 410.5 cm^{-1}) of A_{1g}(M) is close to that (~ 409 cm^{-1}) of $A_{1g}(\Gamma)$, reflecting its dispersionless character.[53,54] The mode ~ 600 cm^{-1} is denoted as E_{2g}^1(M)+LA(M), which leads to E_{2g}^1(M) ~ 367 cm^{-1}. Similar to ~ 178 cm^{-1} (A_{1g}(M)-LA(M)), the mode (E_{2g}^1(M)-LA(M)) is expected at ~ 134 cm^{-1}. However, the obtained LA(M)(~ 232.5 cm^{-1}) is larger than the value determined from $2LA$(M) in non-resonant spectrum (~ 226.3 cm^{-1}). Recently, the double structure of ~ 465 cm^{-1} is re-assigned by Golasa et al. as $2LA$(M) and first phonon replica (E_{1g}(M)+XA(M)) of E_{1g}(M), inspired by the close analogy in profile to the mode at ~ 643 cm^{-1}, which is accordingly assigned as A_{1g}(M)+LA(M) and second phonon replica (E_{1g}(M)+$2XA$(M)) of E_{1g}(M), here XA is related to the transverse acoustic (TA) and/or out of plane acoustic (ZA) mode.[96]

Raman spectrum at low temperature can be used for the identification of two-phonon difference combination mode. Fig.10 demonstrates the Raman spectra of bulk MoS$_2$ at room temperature (upper panel) and at 4K (lower panel). The intensity of a two-phonon mode at $\omega_1 - \omega_2$ will be strongly dependent on temperature as $n(\omega_1, T)[n(\omega_2, T) + 1]$ for creation of a phonon ω_2 and annihilation of ω_1, where $n(\omega, T) = (e^{\hbar\omega/kT} - 1)^{-1}$ is the phonon occupation probability.[97] The intensity of the mode ~ 178 cm^{-1} at 4K is predicted to be a factor of 37 weaker than the intensity at room temperature. Thus, this peak disappears at low temperature, as shown in Fig.10.[96] That is why the mode ~ 178 cm^{-1} is assigned as A_{1g}(M)-LA(M) in Fig.9(b). Moreover, Golasa et al. observed five phonon replicas of E_{1g}(M)(~ 466, ~ 645, ~ 825, ~ 1005 and ~ 1185 cm^{-1}) and A_{2u}(M)(~ 574, ~ 751, ~ 930, ~ 1108 and ~ 1290 cm^{-1}) at 4.2K, as shown in Fig.10 (lower panel). In addition, the mode ~ 782 cm^{-1} (E_{2g}^1(M)+LA(M)+XA(M)) can be considered as the first phonon replica (E_{2g}^1(M)+LA(M)) of ~ 603 cm^{-1}, as shown in Fig.10 (lower panel) by blue line with double arrows. This leads to a series of phonon replicas lying at ~ 962 (E_{2g}^1(M)+LA(M)+$2XA$(M)), 1142 cm^{-1} ((E_{2g}^1(M)+LA(M)+$3XA$(M))) and so on. The resulted frequency of LA(M) is ~ 230.5 cm^{-1}, and XA(M) ~ 180 cm^{-1}. LA(M) approaches the value determined from the non-resonant spectrum, but the attribution of involved XA phonon to M point needs further theoretical analysis.[96] From the phonon dispersion in Ref.54, XA probably corresponds to ZA branch (See Fig.2(c)).

Other bulk MX$_2$ are expected to exhibit similar resonant behaviors to bulk MoS$_2$. However, the resonant excitation energy will be different due to the different band structures. For example, Fan et al. have found that Raman resonance in bulk WS$_2$ covers a large energy range from 1.96 (633nm) to 2.41 (514nm) eV,[101] which is attributed to broad features of its B exciton (ESI-Fig.S4).[102]

5.2 Phonons of monolayer MX$_2$ at Γ and M points
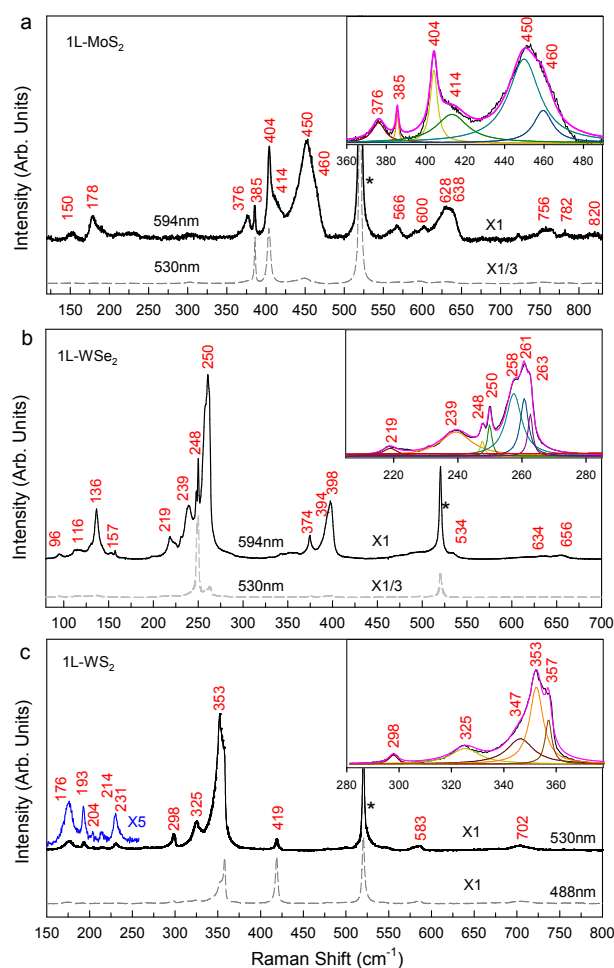

Fig. 11 Resonant (black solid lines) and non-resonant (gray dashed lines) Raman spectra for (a) 1L-MoS$_2$ (b) 1L-WSe$_2$ (c) 1L-WS$_2$ at room temperature. The insets show the sub-peak fitting results. The frequencies of each modes are denoted. The star (*) labels the Raman peak of Si ~ 520 cm^{-1}.

The Raman studies of 1L-MX$_2$ is critical to understand the phonon spectrum of FL-MX$_2$. Fig.11 shows the resonant and non-resonant Raman spectra for 1L-MoS$_2$, 1L-WSe$_2$ and 1L-WS$_2$. The insets show the detailed fitting results for the resonant peaks near $A_1^{'}$ and $E^{'}$. The peak notations in bulk MX$_2$

have been changed in 1L-MX$_2$ due to the different point group (D_{3h}) of 1L-MX$_2$.

In the case of Raman spectrum of 1L-MoS$_2$ in Fig.11(a), the modes lying at ~ 178, ~ 450 and ~ 628 cm^{-1} are assigned as A_1'(M)-LA(M), 2LA(M) and A_1'(M)-LA(M), which is similar to that in bulk.[97,100,103] Similarly, the modes ~ 150 and ~ 600 cm^{-1} are assigned as E'(M)^{LO_2}-LA(M) and E'(M)^{LO_2}+LA(M).[103] Here, E'(M)^{LO_2} is the high-frequency branch of the two splitting branches of E' at M point, E'(M)^{LO_2} and E'(M)^{TO_2}, as shown in Fig.2(b). The mode ~ 600 cm^{-1} is E'(M)^{LO_2}+LA(M) with its second and third phonon replicas found at ~ 638 (E''(M)^{TO_1}+2ZA(M)) and 820 (E''(M)^{TO_1}+3ZA(M)), respectively. The modes ~ 756, ~ 782 and ~ 820 cm^{-1} are 2E'(M)^{LO_2}, E'(M)^{LO_2}+A_1'(M) and 2A_1'(M), which can be used to estimate the spin-orbit splitting in 1L-MoS$_2$ (will be discussed in Section 5.4).[104] It should be noticed that the mode ~ 420 cm^{-1} (B_{2g}^2+E_{1u}^2(Γ-A)) in bulk MoS$_2$ disappears due to the absence of the interlayer breathing mode in 1L-MoS$_2$.

For the Raman spectrum of 1L-WSe$_2$ in Fig.11(b), E'(M)^{LO_2}-LA(M), A_1'(M)-LA(M), 2LA(M), E'(M)^{LO_2}+LA(M), A_1'(M)+LA(M) are found at ~ 116, ~ 136, ~ 261, ~ 374 and ~ 398 cm^{-1}. Besides, the modes ~ 96 and ~ 157 cm^{-1} are E'(M)^{TO_2}-LA(M) and E'(M)^{LO_2}-TA(M), where E'(M)^{LO_2}+LA(M) (expected at ~ 357 cm^{-1}) and E'(M)^{LO_2}+TA(M) (expected at ~ 332 cm^{-1}) are not observed. The combination modes from LA(M), TA(M) and ZA(M) are observed at ~ 219 cm^{-1} (LA(M)+TA(M)), ~ 239 cm^{-1} (LA(M)+ZA(M)) and ~ 263 cm^{-1} (3TA(M)) and ~ 394 cm^{-1} (3LA(M)). The modes ~ 634 and ~ 656 cm^{-1} are E'(M)^{LO_2}+3LA(M) and A_1'(M)+3LA(M), respectively. E'(M)^{LO_2}+2LA(M) and A_1'(M)+2LA(M) are expected to be ~ 504 and ~ 528 cm^{-1}, which is not well-distinguished due to the broad peak range from 460 to 540 cm^{-1} in Fig.11(b).

As for the Raman spectrum of 1L-WS$_2$ in Fig.11(c), E'(M)^{TO_2}-LA(M), E'(M)^{LO_2}-LA(M), A_1'(M)-LA(M), 2LA(M) and A_1'(M)+LA(M) are lying at ~ 176, ~ 193, ~ 231, ~ 353 and ~ 583 cm^{-1}.[65] In addition, the modes ~ 204 and ~ 214 cm^{-1} can be assigned as E''(M)^{TO_1}-ZA(M) and E''(M)^{TO_1}-TA(M). 4LA(M) is also observed at ~ 702 cm^{-1}.[65]

All the tentative assignments of main peaks observed in 1L-MoS$_2$, 1L-WSe$_2$ and 1L-WS$_2$ are summarized in Table.3.

5.3 Layer-dependent resonant Raman scattering in few layer MoS$_2$

The number of atoms in the unit cell of NL-LMs increases with N. More vibrational modes are expected to be involved in the Raman scattering as N increases. Because of the existence of weak interlayer coupling in 2-D LMs, FL-LM each shows distinctive band structure, resulting in the dependency
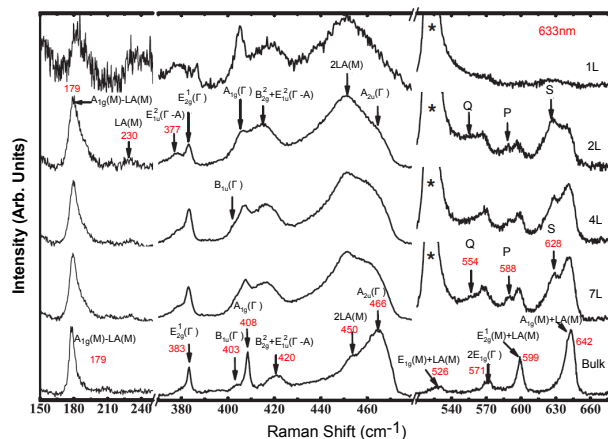

Fig. 12 Resonant Raman spectra of NL- (N = 1, 2, 4 and 7) and bulk MoS$_2$ excited by a 633nm laser. Different modes are indicated with arrows. The symmetry assignments are also addressed for each mode. The noticeable feature is the appearance of completely new modes and their evolution with layer number. Reproduced with permission from ref.105. Copyright 2013, John Wiley & Sons, Inc.

of the corresponding interband transition energy on N. Thus, resonant Raman scattering in 2-D LMs is expected to be layer-number dependent.

Fig.12 shows the resonant Raman spectra of NL- (N = 1, 2, 4 and 7) and bulk MoS$_2$.[105] The strong Raman mode marked by stars(*) is from the SiO$_2$/Si substrate and is completely absent in bulk MoS$_2$. Different notations of the modes in ENL- and ONL- and bulk MoS$_2$ are neglected for the convenience for comparison. The mode assignments in bulk MoS$_2$ can refer those in Section 5.1, except for the observation of B_{1u}(Γ) at ~ 409 cm^{-1} and E_{1g}(M)+LA(M) at ~ 526 cm^{-1}. In the low-frequency spectral region (160-250 cm^{-1}), the lineshape asymmetry of the A_{1g}(M)-LA(M) mode at ~ 179 cm^{-1} are more distinct for N = 2, 4 and 7 because A_{1g} branch is nearly flat and LA branch is concave down at M point (see Figs.2(b) and (c)). An additional peak near 230 cm^{-1} observed in N = 2, 4 and 7 can be assigned as the first-order LA(M). In the spectral region (360-430 cm^{-1}), the mode at ~ 377 cm^{-1} which is broad in 1L becomes sharper in 2L, 4L and 7L. It has been assigned as E_{1u} with a finite wave vector near the Γ along Γ-A (c axis),[105] which is in contrast to the previous assignment to E_{1u}^2(Γ).[98,99] Actually, E_{1u}^2(Γ) is observed on the higher side of E_{2g}^1(Γ).[61] Its relative integrated intensity with respect to E_{2g}^1(Γ) decreases with increasing N, as shown in Fig.12. The prominent peak ~ 420 cm^{-1} is assigned as B_{2g}^2+E_{1u}^2 (Γ-A), which can be used to roughly predict frequency of B_{2g}^2(Γ-A) to be ~ 43 cm^{-1}. B_{1u}(Γ) at ~ 403 cm^{-1} is the Davydov couple of A_{1g}(Γ) (see Fig.2(a)) with its relative intensity to A_{1g} increases with N. The frequencies of 2LA(M) and A_{2u}(Γ) in-

Table 3 Peak positions and their corresponding assignments of each Raman modes observed in 1L-MoS$_2$, 1L-WSe$_2$ and 1L-WS$_2$.

1L-MoS$_2$		1L-WSe$_2$		1L-WS$_2$	
Peak (cm^{-1})	Assignments	Peak (cm^{-1})	Assignments	Peak (cm^{-1})	Assignments
150	$E^{'}(M)^{LO_2}$-LA(M)^a	96	$E^{'}(M)^{TO_2}$-LA(M)	176	$E^{'}(M)^{TO_2}$-LA(M)
178	$A_1^{'}(M)$-LA(M)^a	116	$E^{'}(M)^{LO_2}$-LA(M)^b		or LA(M)^d
376	$E^{'}(M)^{LO_2}$	136	$A_1^{'}(M)$-LA(M)	193	$E^{'}(M)^{LO_2}$-LA(M)^b
385	$E^{'}(\Gamma)^a$	157	$E^{'}(M)^{LO_2}$-TA(M)^c	204	$E^{''}(M)^{TO_1}$-ZA(M)^e
404	$A_1^{'}(\Gamma)^a$	219	LA(M)+TA(M)^c	214	$E^{''}(M)^{TO_1}$-TA(M)^e
414	$A_1^{'}(M)$	239	LA(M)+ZA(M)^c	231	$A_1^{'}(M)$-LA(M)^d
450	2LA(M)^a	248	$E^{'}(\Gamma)^b$	298	$E^{''}(\Gamma)$
460	$E^{''}(M)^{TO_1}$+ZA(M)	250	$A_1^{'}(\Gamma)^b$	325	$E^{''}(M)^{TO_1 e}$
566	$2E^{''}(\Gamma)^a$	258	$A_2^{''}(M)^c$	347	$E^{'}(M)^{TO_2 e}$
600	$E^{'}(M)^{LO_2}$+LA(M)^a	261	2LA(M)^b	353	2LA(M)^d
628	$A_1^{'}(M)$+LA(M)^a	263	3TA(M)^c	357	$E^{'}(\Gamma)^d$
638	$E^{''}(M)^{TO_1}$+2ZA(M)	374	$E^{'}(M)^{LO_2}$+LA(M)^b	419	$A_1^{'}(\Gamma)^d$
756	$2E^{'}(M)^{LO_2 a}$	394	3LA(M)^b	583	$A_1^{'}(M)$+LA(M)^d
782	$E^{'}(M)^{LO_2}$+$A_1^{'}(M)^a$	398	$A_1^{'}(M)$+LA(M)	702	4LA(M)^d
820	$E^{''}(M)^{TO_1}$+3ZA(M)	534	$2A_1^{'}(M)$		
	$2A_1^{'}(M)^a$	634	$E^{'}(M)^{LO_2}$+3LA(M)		
		656	$A_1^{'}(M)$+3LA(M)		

^{a} ref.103. ^{b} ref.72. ^{c} based on the phonon dispersion in ref.63. ^{d} ref.65. ^{e} based on the phonon dispersion in ref.54.

crease with N, but the relative intensity of 2LA(M) to $A_{2u}(\Gamma)$ decreases with N, which is similar to the intensity ratio dependence on the size of nanoparticles[69]. The spectral region between 430 and 490 cm^{-1} is assigned to the second-order Raman spectra, which also show layer dependence with high intensity. The modes $E_{1g}(M)$+LA(M), $E_{2g}^1(M)$+LA(M) and $A_{1g}(M)$+LA(M) have an asymmetrical tail towards low-frequency region, which is due the nearly flat dispersion for E_{2g}^1 and A_{1g} and concave down LA along Γ-M. There are several new peaks $\sim$ 554 (labelled as Q), $\sim$588 (P) and $\sim$628 (S) cm^{-1} in 2L, 4L and 7L, whose peak positions do not vary with N, but their relative intensities with respect to the neighboring modes clearly depend on N.[105] A quantitative understanding of these new features would require theoretical calculations of phonon dispersion and two phonon density of states as a function of N.

5.4 Spin-obit splitting in MoS$_2$ revealed by triply resonant Raman scattering

The sizeable spin-orbit (SO) splitting in 1L-MoS$_2$ is promising in its potential applications in spintronics and quantum information processing, but also makes it a challenge to develop an experimental method to detect and explore intrinsic SOC. Previous attempts were mainly concerned with the energy difference between A and B exciton peaks in the corresponding one-photon (linear)[8] and two-photon (non-linear)[40,41,43] PL spectra. However, the identifications of A and B exciton peaks are still unsettled because of the involvement of an additional
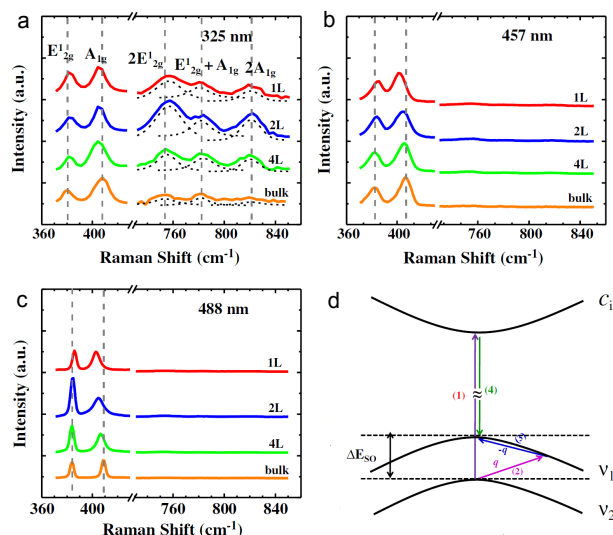

Fig. 13 Raman spectra of 1L-, 2L- 4L- and bulk MoS$_2$ excited by (a) 325, (b) 457 and (c) 488 nm laser lines. All the spectra are normalized by I(A_{1g}). Dashed lines in (a) are the fitting curves. The vertical dashed lines represent the peak positions the Raman modes in bulk MoS$_2$. (d) Schematic diagram for the TRRS process in MoS$_2$, where v_1, v_2 represent the valence band splitting due to spin-orbit interaction, and c_i represents a conduction band. Reproduced with permission from ref.104. Copyright 2013, American Physical Society.

bound exciton peak, which is sensitive to the ambient environment.[14,106] On the other hand, the electron (hole) in CB (VB) band resonantly excited by incident laser could be scattered into a real electronic state by emitting phonon, resulting in double-resonant (DR) or triply resonant (TR) Raman scattering process. Those resonant Raman processes widely exist in the case of graphene.[107] The resonant Raman spectrum is thus very sensitive to the matching between the VB splitting energy and the energy of phonons involved.

Figs.13(a), (b) and (c) show the Raman spectra of 1L-, 2L-, 4L- and bulk MoS_2 excited by 325nm, 457nm and 488 nm laser lines, respectively.[104] Three high-order modes in the range of 750 to 840 cm^{-1} excited by the 325 nm laser are enhanced dramatically and have been assigned as the second order combination Raman modes of E_{2g}^1 and A_{1g}. The three Raman modes are also present in 1L-MoS_2 in Fig.11(a) at $\sim$ 756, $\sim$ 782 and $\sim$ 820 cm^{-1}. The intensity enhancement has been attributed to the electron-two-phonon involved TR Raman scattering (TRRS) process. As illustrated in Fig.13(d), (1) an electron is excited from the v_2 band to c_i band (c_6 band in Ref.104 lying up the band gap) by absorbing a photon at the K point of the Brillouin zone; (2) the hole in the v_2 band is scattered by a phonon with momentum q to the v_1 band by an interband transition as a consequence of deformation potential interaction; (3) another phonon with momentum -q scatters the hole to the top of the v_1 band by intraband transition to form an exciton with the electron in the c_i band due to the Fröhlich interaction[108]; (4) the electron-hole pair recombines at the top of the v_1 band and emitting a photon. For the energy and momentum conservation in TRRS process, one has: $E_{laser} = E_{exciton} + 2E_{E_{2g}^1}$; $E_{laser} = E_{exciton} + 2A_{A_{1g}}$; $E_{laser} = E_{exciton} + E_{E_{2g}^1} + A_{A_{1g}}$ for the different modes $2E_{2g}^1$, $2A_{1g}$ and $E_{2g}^1 + A_{1g}$. The flat phonon dispersion favors the energy and momentum conservation where the right q can be selected in a large range along Γ-M for the right phonon energy ($\Delta E_{SO}/2$), which is responsible for the observing the strong TRRS. In experiment, three resonant high-order peaks excited by 325 nm in 1L-MoS_2 have the energy between 93 meV ($2E_{2g}^1$, actually is $2E'$) and 102 meV ($2A_{1g}$, actually is $2A_1'$), giving a SO splitting $\sim$ 100 meV for 1L-MoS_2.[104] It should be noticed that the splitting in 2L-MoS_2 arises from the combination of SO coupling and interlayer coupling.[8] Much weaker intensities of overtone and combination modes are observed in bulk MoS_2 (Fig.13(a)). Bulk MoS_2 is predicted to have much larger VB splitting which results in a reduction in probability of TRRS due to the loss of energy match between VB splitting and the energy of two-phonons involved.

6 Raman scattering of TMDs modified by external perturbation

External perturbations can modify the electric, phonon, thermal and mechanical properties of 1L-, 2L- and ML-TMDs,[109–114] which facilitates their applications for tunable photonic devices, solar cells, flexible electronics, thermoelectric energy conversion, field effect transistors and catalysts for hydrogen evolution[115]. For example, bandgap engineering through strain is implanted in both 1L- and 2L- MoS_2[113,116]. Chang *et al.* calculated the electronic properties of MoS_2, $MoSe_2$, WS_2 and WSe_2 monolayers and found that their band gaps are more sensitive to biaxial strain.[112] A large value of the Seebeck coefficient is reported for 1L-MoS_2 (-4×10^2 and -1×10^5 μVK^{-1} depending on the strength of external electric field) in thermoelectric energy conversion.[114] Electrical control of neutral and charged excitons in several 1L-TMDs has been recently reported.[117,118] Mitioglu *et al.* observed PL peaks associated with charged excitons of 1L-WS_2 at low temperatures.[119] Pressure-induced phase transition is revealed in MoS_2.[120] TMDs under external perturbation attract much attentions.

Raman spectroscopy is an ideal technology to probe the disturbance of external environmental conditions to material system by means of spectral-feature analysis with high resolution. This makes Raman spectroscopy useful in fundamental research and device characterization. Indeed, phonon spectra of 1L- and ML-TMDs are significantly changed by external perturbation, which allows one to probe their response to external interaction through Raman spectroscopy. In the following, we will discuss in detail how external perturbations such as strain, pressure, electric field, charge transfer, temperature and substrate affect the Raman spectra of TMDs.

6.1 Effect of uniaxial and biaxial strain

One can apply biaxial and uniaxial strains to the sample. Sahin *et al.* recently calculated the phonon dispersion of 1L-WSe_2 after 1% biaxial compressive and tensile strain was applied and found that such biaxial deformation only results in a collective softening/hardening of the vibrational modes and does not lift the degeneracy of the E' and A_1' mode of the 1L-WSe_2.[121] Chang *et al.* further calculated the phonon dispersions of monolayer MoS_2, WS_2, WSe_2 and $MoSe_2$ monolayers and found their phonon frequencies are shifted upward/downward under compressive/tensile biaxial strains.[66] Figs. 14(a) and (b) show the phonon dispersion of 1L-MoS_2 and 1L-WS_2 under unstrain, compressive (bi-axial), tensile (bi-axial), armchair (uni-axial) and zigzag (uni-axial) strain. E' and E'' are degenerate under both compressive and tensile strains, which implies that these modes remain degenerated as long as the hexagonal symmetry of MX_2 is retained. However,
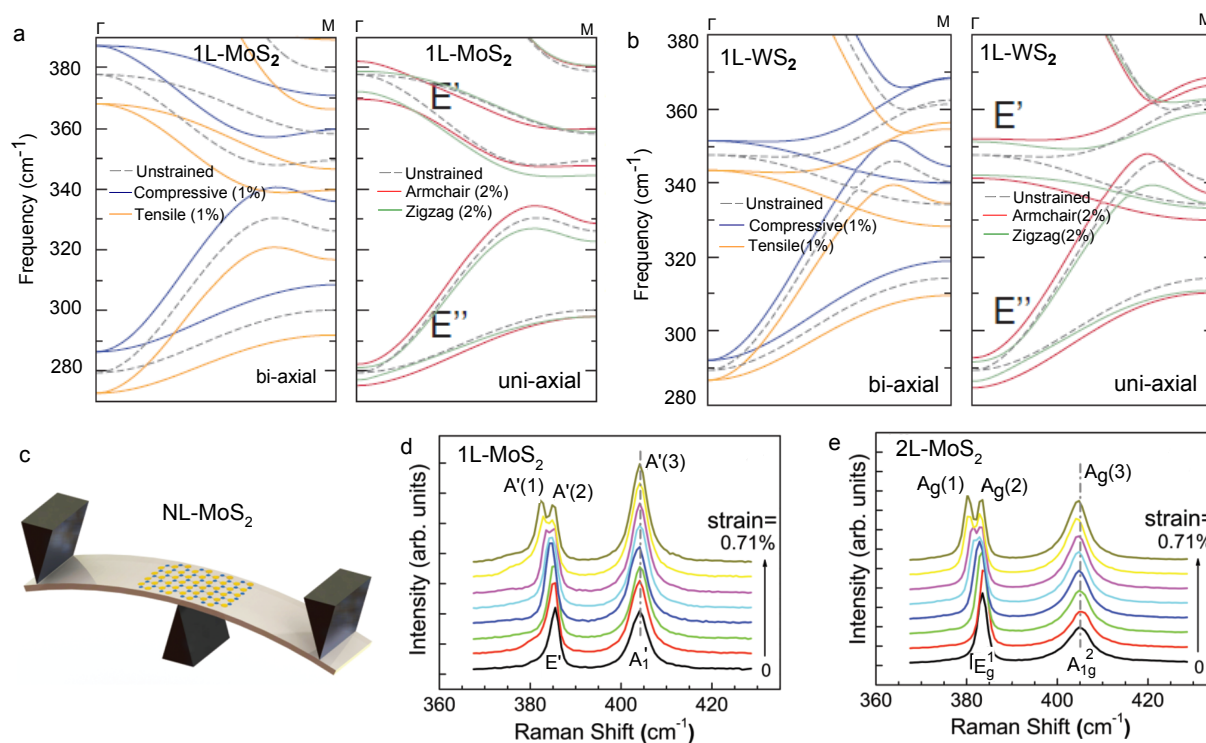
Fig. 14 Phonon dispersions of 1L- (a) MoS_2 and (b) WS_2. For compressive (tensile) bi-axial strains, phonon frequencies of E' and E'' are shifted upward (downward). For uniaxial strains, the degeneracies of E' and E'' at Γ are lifted due to the introduced anisotropy of bond strengths. Reproduced with permission from ref.66. Copyright 2013, American Physical Society. (c) The three-point bending apparatus. (d) E' splits into two modes as tensile strain is applied to 1L-MoS_2. (e) Same as (d) but for 2L-MoS_2. Reproduced with permission from ref.116. Copyright 2013, American Physical Society.

these two modes are split when uniaxial strain is applied , indicating that isotropic symmetry in xy plane has been broken.

A three-point bending apparatus in Fig.14(c) is usually used to apply uniaxial strain to small MX_2 flakes.[116] Zhu *et al.*[116] observed the splitting of E'/E_g^1 with increasing strength of strain in both 1L and 2L under uniaxial strain, as shown in Figs. 14(d) and (e). A_1'/A_{1g}^2 reflect the vibrations along the z axis, whereas E'/E_g^1 describe the vibrations in the xy base plane. In the absence of strain, E'/E_g^1 are 2-D degenerate modes. Applied uniaxial strain will remove the degeneracy due to the symmetry breaking within xy plane, leading to a mode splitting for E' and E_g^1. The lattice symmetry of 1L and 2L changes to C_s and C_{2h} under uniaxial strain, respectively. The corresponding modes are characterized by three A' (1L) and three A_g (2L).[116] For the 1L-MoS_2, with the increase of applied strain, the frequency shift is small for $A'(3)$ mode, indicating that the strain has little effect on the vibration perpendicular to the xy plane (Fig.14(d)). The larger frequency shift of $A'(1)$ with strain signifies that it vibrates along the direction of applied strain. The intensities of the splitted $A'(1)$ and $A'(2)$ orthogonally respond to the angle between the po-

larization of the scattered Raman signal and the strain axis, which can be used to identify crystallographic orientations of 1L-MoS_2.[122] Similar results are also observed in uniaxially-strained 2L-MoS_2 (Fig.14(e)). Moreover, the dispersion of low energy flexural phonons in strained 1L-$MoSe_2$ were found to cross over from quadratic to liner.[62] Based on the strain dependence of $A'(1)$ and $A'(2)$, Conley *et al.* calculated parameters to characterize the anharmonicity of molecular potentials: the Grüneisen parameter, γ, and the shear deformation potential, β. $\gamma_{E'} = 1.1 \pm 0.2$ and $\beta_{E'} = 0.78 \pm 0.1$ are obtained.[113] In addition, strain naturally exists in state-of-the-art for TMD nanotubes, which is similar to MX_2 with uniaxial strains.[123]

6.2 Temperature dependence

Livneh *et al.* reported the temperature and pressure dependence of Stokes and anti-Stokes Raman spectra of bulk 2H-MoS_2, as the energies of the A and B excitons are tuned to resonate with exciting laser.[99] Generally, Stokes scattering peaks are stronger than anti-Stokes scattering peaks with a temperature-dependent intensity ratio, which can practically be exploited for the temperature measurement.[129] Livneh *et*
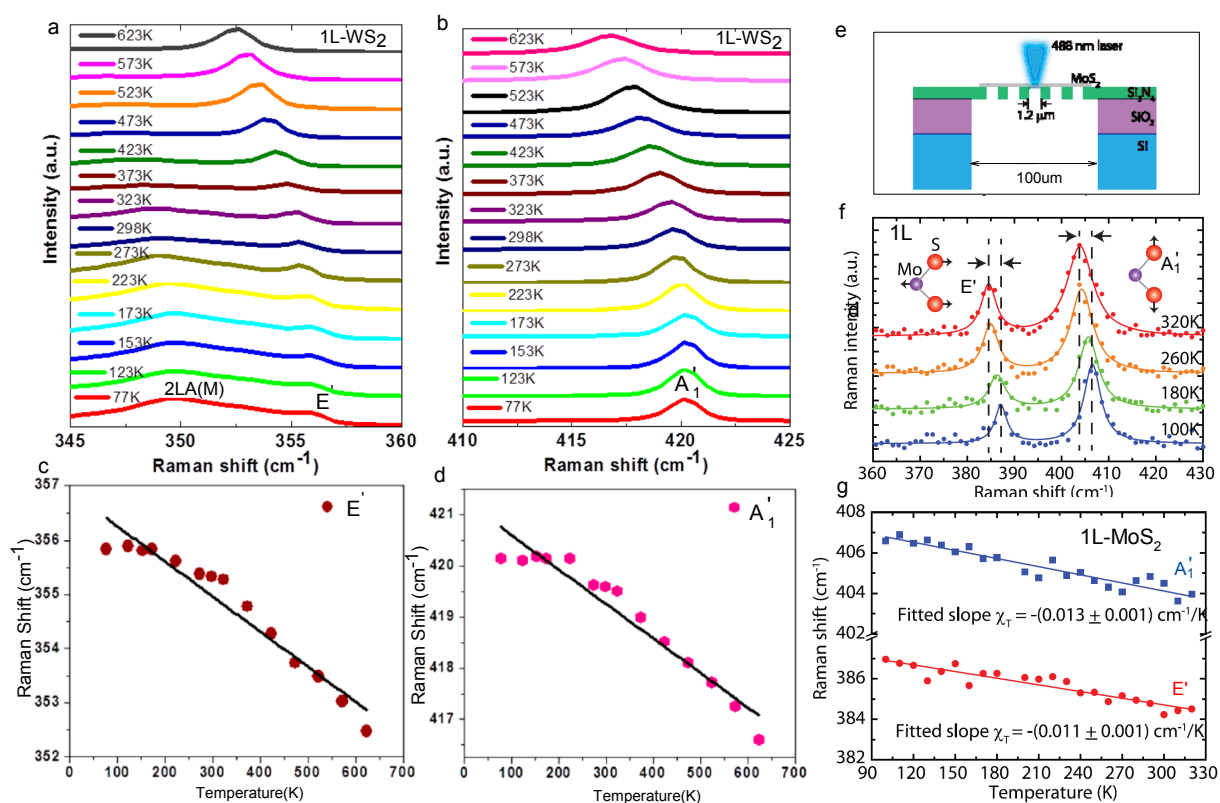
Fig. 15 Raman spectra of 1L-WS$_2$ with (a) E' and (b) A'_1 mode measured in a temperature range from 77 to 623 K, whose Pos(E') and Pos(A'_1) of 1L-WS$_2$ are summarized in (c) and (d), respectively. Adapted from ref.127. (e) Sketch of 1L-MoS$_2$ on Si$_3$N$_4$/SiO$_2$/Si substrate. Here MoS$_2$ over the holes in the 20 nm thick Si$_3$N$_4$ is suspended. (f) Four typical Raman spectra of suspended 1L-MoS$_2$ collected at 100, 180, 260 and 320 K, which are offset vertically for clarity. (g) Raman peak frequencies of both A'_1 (blue squares) and E' (red circles) modes as a function of temperature. Reproduced with permission from ref.125. Copyright 2014, American Chemical Society.

al. found that the absolute values of the temperature coefficients $(\partial \omega / \partial T)_{p=0}$ of the frequency of nearly all modes are roughly within 1.0-1.6×10^{-2} cm^{-1}/K. The temperature coefficient of E^1_{2g} is found larger in magnitude than that of A_{1g} in bulk MoS$_2$, however, in 1L-MoS$_2$,[124] the temperature coefficient of E' is lower in magnitude than that of A'_1, which is intuitively attributed to that no interlayer interactions restrict the vibrations away from the basal plane. Najmaei *et al.* reported the thermal effects induced by laser heating on the Raman spectra of MoS$_2$ with thickness ranging from bulk to 1L.[130] Due to the anomalous trends in frequency for E^1_{2g} and A_{1g}, they found considerable thickness-dependent red-shifts as well as line-width changes for E^1_{2g} and A_{1g} as the laser power increases. The temperature coefficients of 1L-WS$_2$, FL-MoS$_2$ and WS$_2$ in a broader temperature range (77K-623K) are reported by Thripuranthaka *et al.*[126,127] Figs.15(a) and (b) present the temperature-dependent Raman spectra of E' and A'_1 modes whose frequency trends with temperature are summarized in Figs.15(c) and (d), respectively. Both

two modes decrease in frequency with increasing temperature with almost equal temperature coefficient $\sim$ -0.006 cm^{-1}/K. Temperature-dependent Raman spectra of 1L- and FL- WSe$_2$ and MoSe$_2$ is reported by Late *et al.*[128] The obtained temperature coefficients for 1L-, FL- and bulk TMDs are summarized in Table.4.

The negative temperature coefficients (χ_T) in Table.4 are obtained by fitting the peak positions versus temperature using equation: $\omega(T) = \omega_0 + \chi_T T$, where ω_0 is the peak position at zero Kelvin temperature and χ_T is the first-order temperature coefficient. The intrinsic softening with increasing temperature can be attributed to anharmonicity of the interatomic potentials including: (I) contribution from the thermal expansion and (II) phonon-phonon coupling.[131,132] The observed linear evolution of phonon frequencies in 1L-MoS$_2$ has been separately attributed to the thermal expansion[125] and phonon-phonon couplings[124], which needs further experimental and theoretical supports in a larger temperature range. The nonlinear evolution of phonon frequencies in 70-150 K was detected in 1L-MoS$_2$, which was interpreted based on a phenomenon of

Table 4 Comparison of the temperature coefficients (χ_T) for each mode in 1L-, FL- and bulk TMDs.

Material	Type	$E_g^1/E^{'}$ (cm^{-1}/K)	$A_{1g}^2/A_1^{'}$ (cm^{-1}/K)
1L-MoS$_2$	silicon-supported	-0.013[a]	-0.016[a]
1L-MoS$_2$	suspended	-0.011[b]	-0.013[b]
1L-MoS$_2$	sapphire-supported	-0.017[b]	-0.013[b]
FL-MoS$_2$	glass-supported	-0.016[c]	-0.011[c]
Bulk MoS$_2$		-0.013[a]	-0.015[a]
1L-WS$_2$	glass-supported	-0.006[d]	-0.006[d]
FL-WS$_2$	glass-supported	-0.008[c]	-0.004[c]
1L-WSe$_2$	silicon-supported	-0.0048[f]	-0.0032[f]
1L-MoSe$_2$	silicon-supported	-	-0.0054[f]
3L-MoSe$_2$	silicon-supported	-	-0.0045[f]

[a] ref.124. [b] ref.125. [c] ref.126. [d] ref.127. [f] ref.128.

the optical phonon decay of two acoustic phonons with equal energies due to lattice potential anharmonicity.[133] In addition, the temperature-dependent frequency shifts strongly depend on the coupling of TMDs with various substrates.[134]

Yan *et al.* observed the linear softening of both $E^{'}$ and $A_1^{'}$ in suspended 1L-MoS$_2$ with increasing temperature and laser power under 0.25 mW before heating saturation.[125] They obtained thermal conductivity $\kappa =$(34.5$\pm$4) W/mK at room temperature based on the linear temperature and power-dependent coefficients of the $A_1^{'}$ mode. This value is smaller than that reported for the prepared 1L-MoS$_2$ by CVD, $\sim$ 52 W/mK[135] and much smaller than the ultrahigh thermal conductivity (4800-5600 W/mK) of graphene.[136] Cai *et al.* predicted a κ of 23.2 W/mK for 1L-MoS$_2$ by the nonequilibrium Green's function calculations, which is in good agreement with reported (34.5$\pm$4) W/mK.[137] They also calculated Grüneissen parameter (γ) for all acoustic and optical modes at the Γ point. The positive γ suggests a positive coefficient of thermal expansion even at low temperature, which is in contrast to the negative thermal expansion observed in graphene at low temperatures due to the negative γ of the ZA mode.[138,139]

Further, local heating in TMDs flakes induced by laser power has been demonstrated in both supported and suspend 1L-MoS$_2$, where both $E^{'}$ and $A_1^{'}$ soften with increasing laser power (see ESI-Fig.S5).[125,135] Particularly, $E^{'}$ and $A_1^{'}$ soften linearly with increasing power under 0.25 mW, but saturate in the range of 0.25-0.8 mW (see ESI-Fig.S5).[125] The appearance of nonlinear effects results either from the nonlinearity of absorption or higher orders of the temperature-dependent coefficients. Besides, differences in thermal expansion coefficient between TMDs flake and substrate could lead to strain in TMDs, which further enhances the softening effect.

6.3 Phonon renormalization under electric field

A 1L-MoS$_2$ transistor can exhibit an on-off ratio $\sim 10^8$ and an electron mobility of $\sim$ 200 cm^{-2}V^{-1}s^{-1}.[10] Actually, the electronic mobility of semiconductors is limited by the strong electron-phonon interactions which will also have significant effects on phonon frequencies. Recently, Chakraborty *et al.* observed the phonon renormalization of $A_1^{'}$ in 1L-MoS$_2$ transistor.[111] The field effect transistor (FET) and its device performance is demonstrated in Fig.16(a). Fig.16(b) shows the evolution of $E^{'}$ and $A_1^{'}$ of 1L-MoS$_2$ at different top-gate voltages whose frequencies and FWHMs are summarized in Fig.16(c). For a maximum voltage of 2.0 eV, Pos($A_1^{'}$) softens by 4 cm^{-1}, as compared to only $\sim$ 0.6 cm^{-1} for $E^{'}$. The FWHM of $A_1^{'}$ increases significantly by $\sim$ 6 cm^{-1}, whereas no appreciable change happens to $E^{'}$. The gate induced electron concentration (n) can be estimated by $ne = C_{TG}(V_{TG} - V_T)$, where V_T is threshold gate voltage and C_{TG} is top-gate capacitance. Thus, the $A_1^{'}$ mode frequency shift can be used as an readout of the carrier concentration in MoS$_2$ devices.[111] They calculated the electron-phonon coupling (EPC) based on first-principle density functional theory, showing that $A_1^{'}$ couples much more strongly with electrons than the $E^{'}$ mode.[69,111] Actually, the structure distortions due to $A_1^{'}$ do not break the symmetry of MoS$_2$, results in that all electronic states can have a nonzero value in electron-phonon matrix. Electron doping leads the occupation of the bottom of the CB at K point, yielding a significant change in the EPC (λ_n) of A_{1g}. In contrast, the matrix element vanishes for $E^{'}$, resulting in a weak dependence on doping. The phonon linewidth at specific n (Γ_n) is contributed by two different terms, $\Gamma_n = \Gamma^{EPC} + \Gamma^{an}$, where Γ^{EPC} is from EPC contribution and Γ^{an} is contributed from anharmonic effects. The ratio of observed $\Gamma_{n\neq 0}/\Gamma_{n=0}$ is found to follow the calculated strengthening EPC value $\lambda_{n\neq 0}/\lambda_{n=0}$, which indicates that the increasing in FWHM of $A^{'}$ mode (Fig.16(c)) is due to the increase in EPC value with doping.[111]

It should be noted that $A_1^{'}$ renormalization is different from the G-mode renormalization in graphene. The latter is actually due to phonon-induced electron-hole (e-h) pair creation.[140] The phonon-induced e-h pairs are blocked in doped graphene, hence affecting the phonon self-energy. Besides, the G-mode renormalization in graphene is the breakdown of the adiabatic approximation,[141] but $A_1^{'}$ renormalization occurs within adiabatic approximation.

6.4 Substrate effect

TMDs are usually prepared by micro-mechanical exfoliation and transferred on SiO$_2$/Si substrate. Actually, much more conducting (for example, Au and few-layer graphene (FLG)) and insulating (such as, Gel-Film$^{®}$, h-BN flakes and muscovite mica flakes) sample can be taken as substrates.[142]
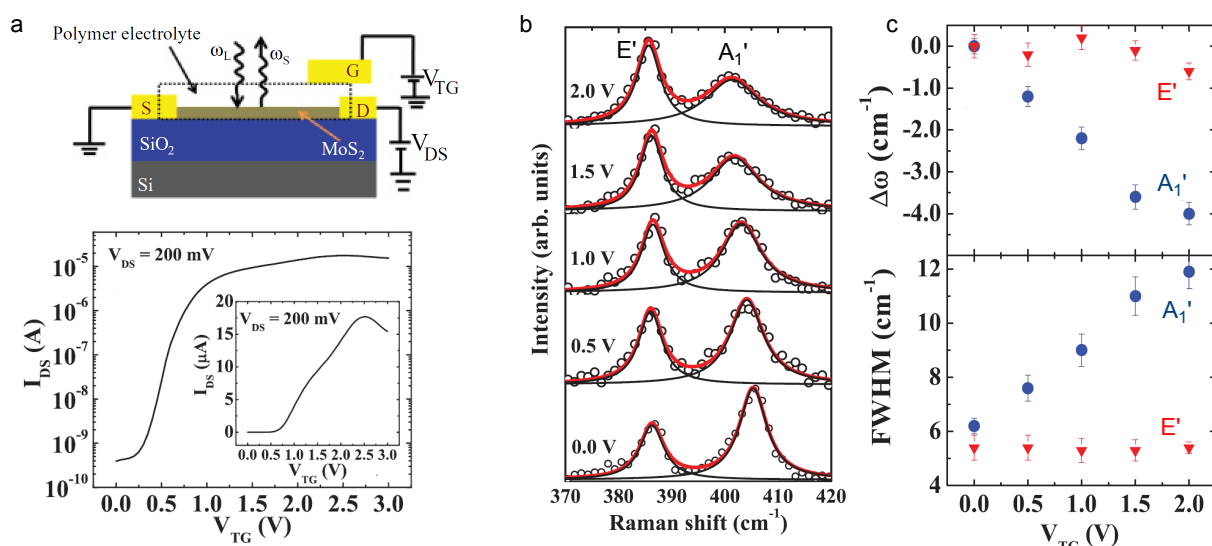
Fig. 16 (a) Schematic of 1L-MoS$_2$ FET and its device performance. (b) Raman spectra of 1L-MoS$_2$ at different top-gate voltages V$_{TG}$. Open circles are experimental data points, the gray (red) lines are Lorentzian fits to the total spectrum, and the black lines are the Lorentzian fit to individual peak. (c) Change of phonon frequency Δ_ω (top) and FWHM (bottom) of A'_1 and E' as a function of V$_{TG}$. Reproduced with permission from ref.111. Copyright 2012, American Physical Society.
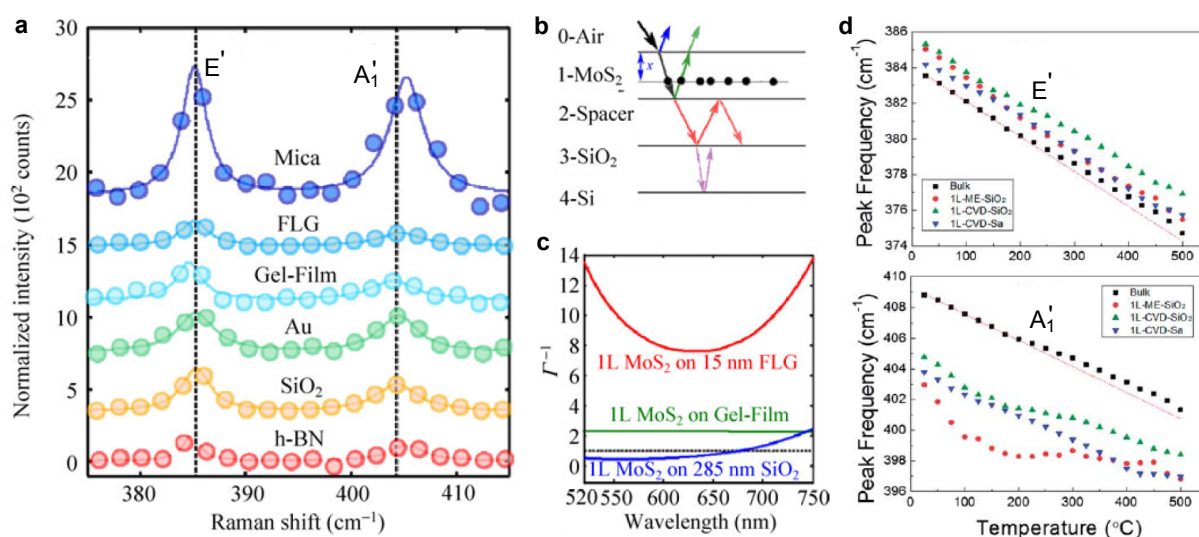

Fig. 17 (a) Normalized Raman spectra for 1L-MoS$_2$ on mica, FLG, Gel-Film®, Au, SiO$_2$ and h-BN, which are shifted vertically for clarity. The dots are the experimental points; the solid lines are Lorentzian fits. The dashed solid lines correspond to Pos(E') and Pos(A'_1) on SiO$_2$. Reprinted from ref.142. (b) Model geometry of optical interference for a heterostructure based on 1L-MoS$_2$. The spacer layer can be Au, FLG, h-BN, or mica. (c) Enhancement factor (Γ^{-1}) as a function of wavelength for 1L-MoS$_2$ on three different substrates. The dashed black line indicates $\Gamma^{-1} = 1$. Temperature dependence of (d) E' and (e) A'_1 of bulk, CVD-grown 1L-MoS$_2$ on sapphire (1L-CVD-sa), the transferred one from CVD-grown 1L-MoS$_2$ on SiO$_2$/Si (1L-CVD-SiO$_2$) and 1L-MoS$_2$ on SiO$_2$/Si by directly mechanical exfoliation from bulk (1L-ME-SiO$_2$). Reproduced with permission from ref.143. Copyright 2014, Royal Society of Chemistry.

Fig. 17(a) presents E' and A'_1 of 1L-MoS$_2$ on six different substrates. The intensities of E' and A'_1 modes are clearly modulated by the substrate, which needs account for optical interference and absorption effects, as depicted in Fig.17(b) for

MoS$_2$ laid on SiO$_2$/Si substrate. The Raman intensity of 1L-MoS$_2$ lying on SiO$_2$(285 nm)/Si is expected to be strong than that on both Gel-Film and 15nm FLG, as shown in Fig.17(c). It should be noted that this interference effect of the substrate

dose not shift the peak position. However, A_1' shows a sizeable stiffening of up to ~ 2 cm^{-1} with varying substrates in the sequence of SiO$_2$, Au, Gel-Film, FLG, Mica and h-BN, while E' is barely affected by the substrate, as indicated in Fig.17(a). Two possible explanations can be accounted for this stiffening: charge transfer between 1L-MoS$_2$ and substrate[111], and dipolar interaction between 1L-MoS$_2$ and the fixed charges in the different substrates.[142]

The temperature behaviors of A_1' and E' of 1L-MoS$_2$ is also dependent on substrate.[143] Strong nonlinearity on the temperature shift of A_1' is observed in 1L-MoS$_2$ on sapphire and SiO$_2$ (Fig.17(d)), while that of E' is almost linear. This nonlinearity can be associated with likely chemical bonding between film and substrate, and also mismatch in thermal expansion between the film and substrate.

6.5 Pressure-induced semiconducting to metallic transition

TMDs with lattice distortions by applying external pressure are predicted theoretically to undergo a semiconductor to semimetal transition and even full metallization.[145–147] The metallization arises from the overlap of the valance and conduction bands as interlayer spacing reduces. Recently, both x-ray diffraction (XRD) and Raman spectroscopy of ML (at ~ 19 GPa) and bulk MoS$_2$ (between 20GPa and 30GPa) under high pressure verified the above transitions.[99,120,148]

Fig.18(a) presents the Raman spectra of bulk MoS$_2$ at various pressures up to 57 GPa in both compression (denoted by c) and decompression (denoted by d) run.[120] Both E_{2g}^2 and E_{2g}^1 develop new split-off features when the applied pressure is above 23.0 GPa. The splitting of E_{2g}^1 was also reported to begin at 19.1 GPa.[99] Further, E_{2g}^2 is directly associated with interlayer stacking. Its splitting indicates the existence of new phase due to layer sliding. This new phase at high pressure is denoted by $2H_a$ whose lattice parameter c drops down compared to that of normal $2H$ phase (denoted by $2H_c$ in Ref.120). $2H_a$ is a metallic state, as revealed by the temperature-dependent resistivity. The two separate peaks for both E_{2g}^2 and E_{2g}^1 in bulk $2H_c$ totally disappear around 40 GPa, indicating that the transformation from $2H_c$ to $2H_a$ is complete. Upon decompression, Raman modes from $2H$ come up, which indicates the reversibility of $2H_c$ and $2H_a$ phase. Figs.18(b), (c) and (d) summarize the data for the pressure dependence of the frequencies of E_{2g}^2, E_{1g}, A_{1g}^1 and E_{2g}^1.[99,144,145] Discontinuities are revealed for Pos(E_{2g}^2) and Pos(E_{2g}^1) at beginning of phase transition (about 20 GPa), but not for Pos(E_{1g}) and Pos(A_{1g}^1). The discontinuities of Pos(E_{2g}^2) and Pos(E_{2g}^1), together with that of frequency difference, Pos(A_{1g}) $- Pos(E_{2g}^1$) (Fig.18(e)), clearly divide the phase into three parts, ie, $2H_c$, $2H_a$ and the coexistence of them.

7 Applications of ULF Raman spectroscopy in 2-D layered materials

7.1 Substrate-free characterization of layer number for multilayer TMDs

The properties of 2-D TMDs and other layered materials significantly depend on their layer number, N, which is a prerequest for their potential applications. It requires a reliable and rapid characterization technique for ultrathin 2-D TMDs. The methods such as optical contrast, atomic force microscopy (AFM), photoluminescence (PL) and Raman spectroscopy have been widely used as characterization tools.

Optical contrast is initially the most powerful characterization tool for 1L and ML graphenes[149] and TMDs[48]. Optical contrast ($\delta(\lambda)$) is defined as $1-I_{flake}(\lambda)/I_{sub}(\lambda)$, where $I_{flake}(\lambda)$ and $I_{sub}(\lambda)$ are the reflected light intensity at flake and substrate, respectively.[48,150,151] To precisely identify N, one must compare the experimental optical contrast with the theoretical one with different layer number. In the calculation of optical contrast, the number aperture of the used objective, the thickness of 1L flake, the thickness of the dielectric layer (usually SiO$_2$) on substrate and complex refractive index of the flakes are necessary to give a reliable theoretical result. However, the refractive index and its monolayer thickness of many novel layered materials is unknown. The thickness of the SiO$_2$ layer provided by a company is usually with an error of $\pm5\%$. In this case, optical contrast is not so easy for layer-number identification of novel layered materials. In Fig.19(a), we show the evolution of optical contrast of 1L- to 8L-MoWS$_2$ deposited on 90nm SiO$_2$/Si. It is obviously difficult to match the theoretical curve with the experimental one to identify its layer number because the refractive index of the flakes is sensitive to its layer number.

Atomic force microscopy (AFM) is a direct and powerful technique to identify layer number with a precision of 5%.[152] However, the different interactions of AFM tip with the flake and with substrate will lead to discrepancies in the layer number.[153] Also, the precision of AFM measurement is subject to the substrate roughness and the cleanliness of flake surface. Indeed, in Fig.19(b), 4L- and 5L-MoWS$_2$ can be clearly identified in the optical image. However, the accidental glue spots, rough surfaces and substrate make it unable to accurately determine the layer number of this real flake in Fig.19(b), as shown by its AFM image (Fig.19(c)) and the height profile across 4L- and 5L-MoWS$_2$ (Fig.19(d)).

Photoluminescence (PL) is based on the evolution of peak position or peak intensity of PL peaks on the flake thickness.[8,9] MoS$_2$ is undergoing from indirect bandgap in bulk to direct bandgap in 1L, which also happens in WS$_2$, WSe$_2$ and MoSe$_2$.[26] The transition leads to an enhanced PL emission in 1L and weaken PL intensity as N increases. PL signal is nor-
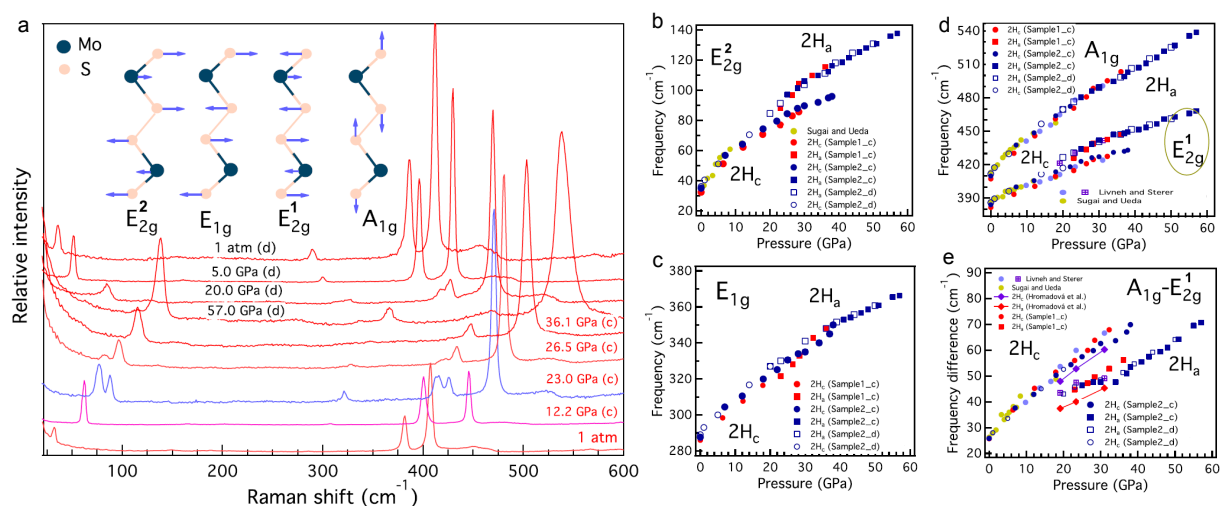
Fig. 18 (a) Raman spectra of MoS$_2$ at various pressures up to 57 GPa in both the compression (denoted by c) and decompression (denoted by d) runs. The insets represent in-plane modes E_{2g}^2, E_{1g}, and E_{2g}^1 and the out-of-plane mode A_{1g}. (b) Pos(E_{2g}^2), (c) Pos(E_{1g}), (d) Pos(E_{2g}^1) and Pos(A_{1g}), and (e) Pos(A_{1g})-Pos(E_{2g}^1) of MoS$_2$ as a function of pressure. The solid and open symbols are the data for the compression and decompression runs, respectively. The experimental (refs.99, 144) and theoretical (ref.145) data are shown for comparison. $2H_c$ and $2H_a$ corresponds to the low-pressure and high-pressure phases, respectively. Reproduced with permission from ref.120. Copyright 2014, American Physical Society.
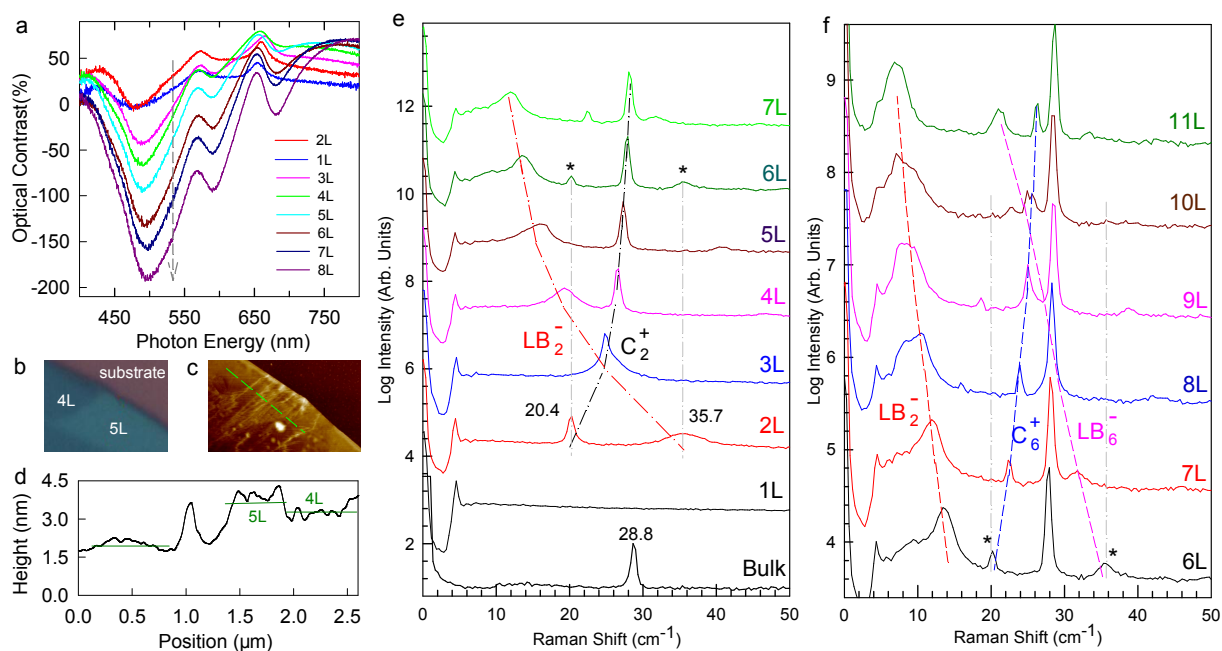

Fig. 19 (a) Optical contrast as a function of N for NL-MoWS$_2$ supported on 90 nm thick SiO$_2$/Si substrate. (b) Optical and (c) AFM images for 4L- and 5L-MoS$_2$; (d) height profile along dashed green lines in (c). Raman spectra of (e) 1-7L and (f) 6-11L MoWS$_2$. The dashed lines in (e) and (f) are guides to the eye.

mally used as a rapid characterization of 1L- and 2L- TMDs with high crystal quality. Because PL emission is very sensitive to the temperature, defect and doping, it is not efficient to identify layer number for thicker flakes or for 2-D LMs without PL emission.

Raman spectroscopy has been a nondestructive and

high-throughput characterization method for 1L and ML graphene [17,84,107,154–158] and shown its potentials in general 2-D layered materials. [18,75,159] The anomalous frequency trends for E_{2g}^1 and A_{1g} modes in 1-6L and bulk MoS$_2$,[18] as shown in Fig.4, can be used for their layer thickness determination for 1-5L MoS$_2$ and WS$_2$. However, it is not sensitive for the MoS$_2$/WS$_2$ flakes with layer number larger than 5L. Also, for other 1L- and ML-MX$_2$, the frequency difference between E_{2g}^1 and A_{1g} dependent on the layer number is needed for reconstruction, during which the layer number must be determined initially by other methods.

It is essential to demonstrate a substrate-free approach to identify the layer number of 2-D LM flakes, which is not bound up with the refractive index, monolayer thickness, PL emission and high-frequency optical modes of the material. As discussed in Section 4.2, the peak positions and number of C and LB modes significantly depend on the layer number of the MX$_2$ flakes. [159] In the following, we will discuss how to identify the layer number of MoWS$_2$ alloy, whose physical properties have not been well-known yet.

By mechanical exfoliation, we obtained a series of MoWS$_2$ flakes with different thickness. [160] At first, when we measure the ULF Raman modes of bulk MoWS$_2$, we can get the C mode at 28.8 cm^{-1}, as shown in Fig.19(e). There is no any Raman signal in the C mode range for the flake with smallest optical contrast. It could be assigned as 1L-MoWS$_2$ because the C mode does not exist in 1L-MoWS$_2$. Another flake only shows two ULF Raman modes at 20.4 cm^{-1} and 35.7 cm^{-1}, respectively. Note that C mode at 20.4 cm^{-1} is exactly $1/\sqrt{2}$ times as much as that (28.8 cm^{-1}) of bulk sample. According to the MCM in Section 4.2, the flake is 2L-MoWS$_2$ and another mode at 35.7 cm^{-1} is the LB mode of 2L-MoWS$_2$. Then, the C and LB frequencies of NL-MoWS$_2$, respectively, follow the equations of $\omega(C_2^+)(N) = C(2)\sqrt{1+cos(\pi/N)}$ $(N \geq 2)$ and $\omega(LB_2^-)(N) = LB(2)\sqrt{1-cos(\pi/N)}$ $(N \geq 2)$. We measure ULF Raman modes of thicker MoWS$_2$ flakes, as summarized in Fig.19(e). By comparing the theoretical frequencies of C and LB modes with the experimental ones, we can identify the layer number of thicker MoWS$_2$ flakes. However, as shown in Fig.19(e), when $N > 7$, $\omega(LB_2^-)(N)$ exhibits a lineshape different from the Lorentzian one, and the frequency difference of $\omega(C_2^-)(N)$ between sequential layers will be too small to be distinguished with each other because of the limit of spectral resolution. The phonon branches of C_2^+ and LB_2^- can not be further used for layer identification of $N > 7$ any more. As demonstrated in Fig.19(f), we can consider another phonon branches of C_6^+ and LB_6^- and the corresponding C and LB frequencies, respectively, follow the equations of $\omega(C_6^+)(N) = C(2)\sqrt{1+cos(3\pi/N)}(N \geq 6)$ and $\omega(LB_6^-)(N) = LB(2)\sqrt{1-cos(3\pi/N)}$ $(N \geq 6)$. One can also consider the phonon branches of C_{10}^+ and LB_{10}^- further for higher layer-number identification. In fact, the above ap-
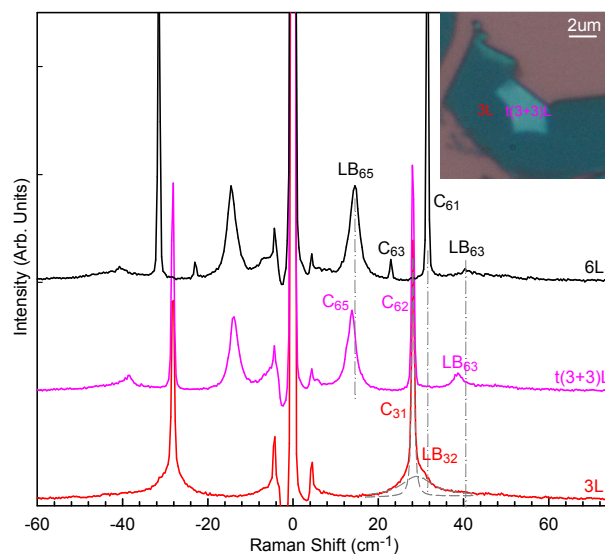

Fig. 20 ULF Raman spectra of t(3+3)L, together with 2H-stacked 3L- and 6L- MoS$_2$. Inset shows the optical image for the t(3+3)L- and 3L- MoS$_2$. Dash-dotted lines indicate Pos(LB$_{63}$), Pos(C$_{63}$) and Pos(LB$_{65}$) in 2H-stacked 6L-MoS$_2$.

proach can be robust for any 2-D LMs once we can detect the C and LB modes of the material.

7.2   Probing the interface coupling in folded TMDs

Interface coupling is emerging as a powerful method to engineer physical properties of atomically thin two-dimensional materials. New physical phenomena including new van Hove singularities, [161–163] Fermi velocity renormalization [164] and unconventional quantum Hall effects [165] has been revealed in graphene bilayers and graphene/boron nitride heterostuctures. Several attempts has been devoted to folded MoS$_2$ bilayers to study how the interface coupling will affect its optical emission, exciton and valley polarization. [166–168] The indirect bandgap varies appreciably with the stacking configuration, where it shows the largest redshift for AA- and AB-(2H) stacked bilayers, and a significantly smaller but constant redshift for all other twist angles. [167] Further, strong valley and spin polarization is achieved in folded MoS$_2$ bilayers. [168]

From the results in Section 4.2, C and LB modes are directly related to the interlayer coupling, which can be used to probe the interface coupling in folded TMDs. Here, we present the C and LB modes in 3L-MoS$_2$ folded by another 3L-MoS$_2$ on its top. This twisted 6L-MoS$_2$ is denoted by t(3+3)L-MoS$_2$. In NL-MoS$_2$, there are N-1 C modes, which we indicate as C$_{NN-i}$, with i=1,...,N-1. In this notation, for a given N, the label C$_{N1}$ is used for the highest frequency C peak. Similar notation can be used for N-1 LB modes in NL-MoS$_2$. Optical image of the t(3+3)L is shown in the inset to Fig.20, whose 3L

constituent can be verified by its C (C_{31} at 29.2cm^{-1}) and LB (LB_{32} at 28.1cm^{-1}) modes, as shown in Fig.20. Fig.20 also present the Raman spectrum of 2H-stacked 6L-MoS_2, where C_{61}, C_{63}, LB_{63} and LB_{65} are detected, in agreement with the results in Figs.3 and 6. However, t(3+3)L-MoS_2 exhibits a quite different Raman spectrum from that of both 3L- and 6L-MoS_2. LB_{63} and LB_{65} are observed in t(3+3)L-MoS_2 with lower frequency than those in 6L-MoS_2, howsoever, the corresponding C_{61} and C_{63} in 6L-MoS_2 are absent in t(3+3)L-MoS_2 with a presence of C_{62}. Based on the linear chain model, we find that the interlayer coupling constant at the twisted interface ($\alpha_t^\perp$) follows: $\alpha_t^\perp/\alpha_0^\perp$=95%, here $\alpha_0^\perp$ is the interlayer coupling constant in 2H-stacked MoS_2 for LB modes. It directly indicates that the interlayer coupling is reduced at the twisted interface. Obviously, the LB modes here make themselves the direct probe of the interface coupling in folded (or twisted) TMDs.

8 Perspective of the study on layered materials

8.1 Other 2-D materials beyond TMDs

In parallel with the researches on graphene-like materials, TMDs received growing interests, which will promote next studies on other 2-D materials. Geim and Grigorieva built a current 2-D library, including three families: Graphene family (graphene, hBN, graphene oxide...), 2-D chalcogenides (MoS_2, WS_2, $MoTe_2$, GaSe, Bi_2Se_3...) and 2-D oxides (WO_3, layered Cu oxides, MnO_2...), as shown in Fig.21(a).[169] Although several achievements have been made in Bi_2Se_3/Bi_2Te_3[172,173], GaTe[174], GaS[175], GaSe[175], InSe[176,177], CuSe[178] and ReS_2[170], a large number of these 2-D materials, especially in ultra-thin scale, are still waiting for explorations.

Raman spectroscopy will continuously gain our knowledge of unique properties of these 2-D materials. For example, ReS_2, in contrast to TMDs, is found to remain direct bandgap from bulk to monolayer and its Raman spectrum shows no dependence on the layer number (Fig.22(a)), which is due to electronic and vibrational decoupling.[170] The topological insulators Bi_2Se_3 and Bi_2Te_3 hold low-frequency modes which are different from interlayer C and LB modes, as shown in Fig.22(b). The out-of plane A_{1g}^1 mode located at ~ 72 cm^{-1} in bulk Bi_2Se_3 exhibits a sensitive red shift as the thickness decreases due to phonon softening.[173] A significant broadening of the in-plane E_g^2 mode is also identified as the thickness decreases, resulting from a decrease of the phonon lifetime of the intralayer modes, possibly due to an enhanced electron-phonon coupling.[173] Fig.21(c) shows the Raman spectra of thin (29 nm) and bulk GaSe under both XX and YX configurations.[175] In bulk GaSe (upper panel), those modes present under both XX and YX are E_{1g} and E_{2g}, while the modes only

present under XX are A_{1g}. The polarization and peak position of each mode in FL-GaSe (29 nm) are similar to those in bulk GaSe, indicating good crystal structure. However, a significant decreasing in intensity of Raman vibrations can be seen from the signal-to-noise of the Raman spectra of FL-GaSe flakes (lower panel), which is different to the case of MoS_2, where Raman spectra of 45L-MoS_2 (~ 29 nm) is identical to that of bulk.

8.2 van der Waals Heterostructures

Various 2-D materials could be "restacked" or assembled vertically in a chosen sequence (Fig.21(b)) to form various hybrids and heterostructures, creating materials on demand, which will provide fine-tuned properties and new opportunities for devices.[179–181] These hybrids and heterostructures are vividly referred to as van der Waals heterostructures, where strong covalent bonds provide in-plane stability of 2-D crystals, whereas relatively weak, van-der-Waals-like forces are sufficient to keep the stack together.

Graphene/MoS_2 heterostructure firstly synthesized by Chang et al.[182] stimulates growing works on its applications in electronics and optoelectronics due to the semiconductivity of MoS_2 and high conductivity of graphene. Now, more exciting works are devoted to exploring the heterostructures fabricated by various TMDs. Before the extensive production of TMD heterostructures, several theoretical works have been implanted to study their electronic structures.[35,183–186] For example, Kośmider et al. found that the band gap in 1L-MoS_2/1L-WS_2 heterostructure is direct, which is in contrast to both 2L-MoS_2 and 2L-WS_2. Additionally, the lowest energy electron and highest energy hole states in the optically active K point are localized on different monolayers, i.e., electron-holes pairs are spatially separated.[185] Kang et al. calculated Moiré pattern effects on the electronic structure of 1L-MoS_2/1L-$MoSe_2$ heterostructure and found that VBM state is strongly localized while CBM state is only weakly localized.[183] The experimental works are growing, and preliminary results have been obtained.[187–190]

The interlayer coupling, strain, charge transfer, lattice vibrations, and interface diffusion within heterostructures and hybrids will change the band structure, Fermi level, and band offsets. Raman scattering as a nondestructive measurement at room temperature under ambient pressure is ideal to probe the variation of properties from those of the constituent materials. Indeed, Raman scattering was applied in twisted BLG to reveal changes in band structure, with appearance of angle-dependent van Hove singularities.[163] Because the interactions between different layers inside heterostructures and hybrids are much weak due to van der Waals forces holding them together, the vibrations of heterostructures and hybrids will consist of those from the individual building blocks. Therefore,
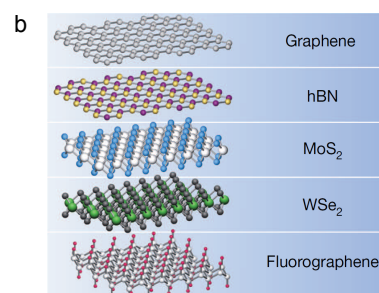
Fig. 21 (a) Current 2-D library. Monolayers proved to be stable under ambient conditions (room temperature in air) are shaded blue; those probably stable in air are shaded green; and those unstable in air but that may be stable in inert atmosphere are shaded pink. Grey shading indicates 3-D compounds that have been successfully exfoliated down to monolayers. (b) Building van der Waals heterostructures. Reproduced with permission from ref.169. Copyright 2013, Nature Publishing Group.
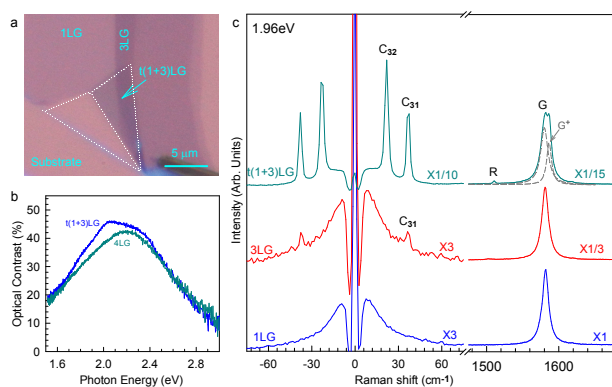

Fig. 23 (a) Optical image of a graphene flake containing 1LG, 3LG and t(1+3)LG. (b) Optical contrast of t(1+3)LG and Bernal-stacked 4LG. (c) Raman spectra of 1LG, 3LG and t(1+3)LG in the C and G peak range excited by 1.96 eV. The G^+ mode is clearly identified by the fit to the t(1+3)LG G band. Reproduced with permission from ref.81. Copyright 2014, Nature Publishing Group.

Raman spectroscopy is expected to be useful to probe the stoichiometry of heterostructures and hybrids. For example, the Raman peaks from graphene and $FeCl_3$ can be identified in $FeCl_3$-intercalated FLGs,[191] while at the same time probing the layer coupling, stability, charge transfer, strain, and orientation.[191] E' and A_1' modes from 1L-MoS_2 and 1L-WS_2 are all observed in the Raman spectra of MoS_2/WS_2 heterostructure, indicative of forming a 1L-MoS_2/1L-WS_2 heterostructure.[188] C and LB modes are mainly determined by the weak interlayer interactions, thus will be an effective tool to probe the interlayer coupling in heterostructure[192]. Raman spectroscopy can also be used to monitor/optimize growth conditions for heterostructures and hybrids.[193]

Before the attempts on TMDs heterostructure, several advances of ULF Raman spectroscopy has been made in twisted multilayer graphene.[81,194] Fig.23(a) shows the optical image of a flake which contains monolayer graphene (1LG), trilayer

graphene (3LG) and twisted (1+3) layer graphenes(t(1+3)LG). Here, $t(m+n)$LG refers to artificially assembling m-layer graphene (mLG, $m \geq 1$) on n-layer graphene (nLG, $n > 1$), where the mLG and nLG can be twisted by an angle θ_t with respect to each other. θ_t between the layers can be used to tune the optical and electronic properties of the twisted system.[161,195] The optical contrast of t(1+3)LG shown in Fig.23(b) is quite different from that of 4LG. An additional feature appears at around 2.0 eV for t(1+3)LG, revealing that the band structure of twisted t(1+3)LG is modified after twisting in comparison to Bernal-stacked graphene layers. Fig.23(c) shows the Raman spectra of 1LG, 3LG and t(1+3)LG in the C and G peak region. There is an additional G^+ peak in t(1+3)LG, and the G peak in t(1+3)LG is enhanced in intensity, suggesting a weak coupling between 1LG and 3LG constituents in t(1+3)LG. The C mode of 3LG is observed at 37 cm^{-1} (C_{31}).[80] Another C mode at 22 cm^{-1} (C_{32})[17,80] is not observable in 3LG. The t(1+3)LG contains four layers. In Bernal-stacked 4LG, three C modes are expected at 41 (C_{41}), 31 (C_{42}) and 17 (C_{43}) cm^{-1}.[17,80] However, only two C modes at 22 cm^{-1} and 37 cm^{-1} are observed in t(1+3)LG, whose frequency is close to that of 3LG. The observation of C_{31} and C_{32} in t(1+3)LG shows that the weaker interlayer coupling between 1LG and 3LG constituents in t(1+3)LG makes the C mode vibration mainly localized in the 3LG constituent. Also, the C_{31} intensity in t(1+3)LG excited by 1.96 eV is significantly enhanced by about 100 times in comparison to that in 3LG. All the above results demonstrate that the peak position and intensity of the C modes in $t(m+n)$LG is very sensitive to probe the interlayer coupling at the interface of $t(m+n)$LG,[81] which paves way for fundamental understanding into the interface coupling of van der Waals interface coupling in 2-D crystal based heterostructures.
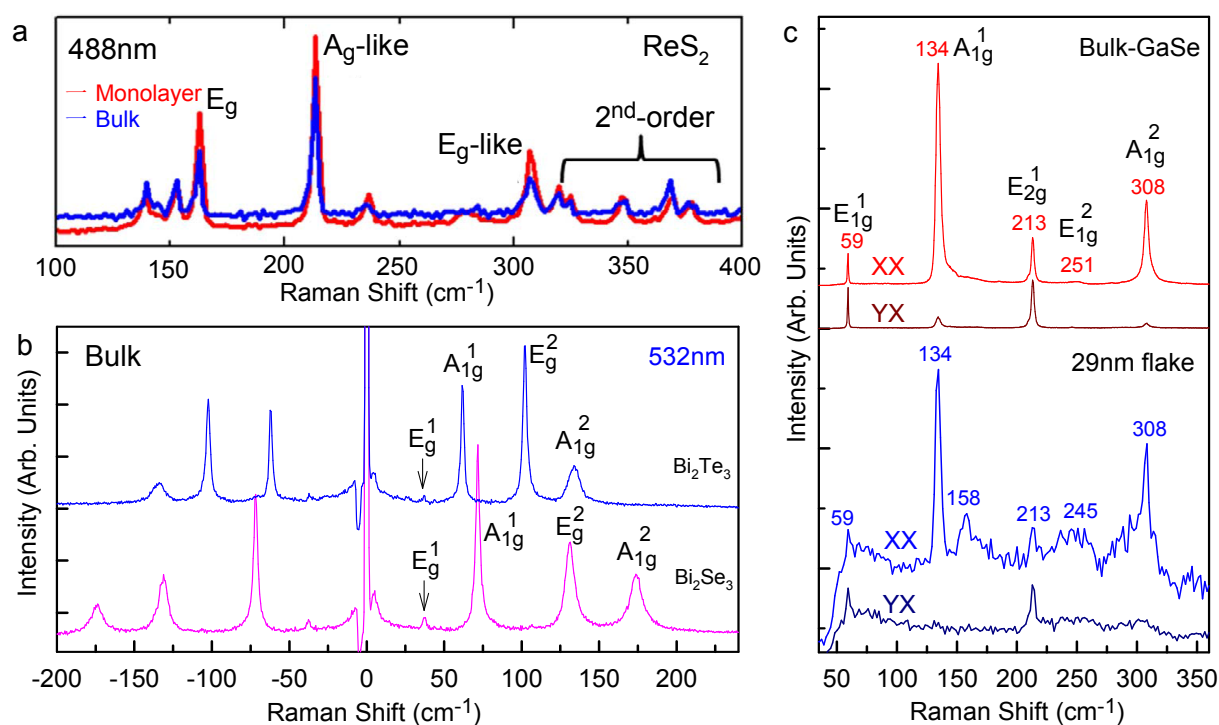
Fig. 22 (a) Raman spectra of bulk (blue) and monolayer (red) ReS_2. Reproduced with permission from ref.170. Copyright 2014, Nature Publishing Group. (b) Raman spectra of bulk Bi_2Se_3 and Bi_2Te_3. (c) Polarized Raman spectra of bulk GaSe (top) and a 29nm flake (bottom). Reproduced with permission from ref.171. Copyright 2014, American Chemical Society.

9   Conclusion

2-D layered TMDs with extraordinary electronics, spintronics, valleytronics, optoelectronics and appealing applications in devices will stimulate much progress in this field. We mainly reviewed the phonon structure of type MX_2 from 1L, ML to bulk and the extensive capabilities of Raman spectroscopy in studying the properties of various TMDs. Non-resonant Raman scattering has made advances in characterization of layer number, phonon structure at and around Γ points, probing interlayer coupling and determination of alloy composition and degree for various 2-D crystal alloys. Resonant Raman spectroscopy has potentials in studying the phonon structure at M point or along non-planar direction, and intrinsic spin-orbit coupling in valence band. Both non-resonant and resonant Raman spectroscopy can be used to investigate the effect on TMDs from external perturbation, such as strain, temperature, pressure, charge transfer and electric field. We further demonstrated that Raman spectroscopy is expected to be an effective tool for TMDs-based van der Waals heterostructures and other 2-D materials beyond TMDs. In particular, the measurement of C and LB modes will develop our knowledge on the interface coupling in various van der Waals heterostructures.

10   Acknowledgments

References

1 K. S. Novoselov and A. H. Castro Neto, *Phys. Scr.*, 2012, **2012**, 014006.

2 F. Bonaccorso, A. Lombardo, T. Hasan, Z. Sun, L. Colombo and A. C. Ferrari, *Materials Today*, 2012, **15**, 564–589.

3 J. N. Coleman, M. Lotya, A. ONeill, S. D. Bergin, P. J. King, U. Khan, K. Young, A. Gaucher, S. De, R. J. Smith, I. V. Shvets, S. K. Arora, G. Stanton, H.-Y. Kim, K. Lee, G. T. Kim, G. S. Duesberg, T. Hallam, J. J. Boland, J. J. Wang, J. F. Donegan, J. C. Grunlan, G. Moriarty, A. Shmeliov, R. J. Nicholls, J. M. Perkins, E. M. Grieveson, K. Theuwissen, D. W. McComb, P. D. Nellist and V. Nicolosi, *Science*, 2011, **331**, 568–571.

4 Q. H. Wang, K. Kalantar-Zadeh, A. Kis, J. N. Coleman and M. S. Strano, *Nat. Nanotechnol.*, 2012, **7**, 699–712.

5 M. Chhowalla, H. S. Shin, G. Eda, L. J. Li, K. P. Loh and H. Zhang, *Nat. Chem.*, 2013, **5**, 263–275.

6 M. Xu, T. Liang, M. Shi and H. Chen, *Chemical Reviews*, 2013, **113**, 3766–3798.

7 J. A. Wilsona and A. D. Yoffea, *Adv. Phys.*, 1969, **18**, 193–335.

8 K. F. Mak, C. Lee, J. Hone, J. Shan and T. F. Heinz, *Phys. Rev. Lett.*, 2010, **105**, 136805.

9 A. Splendiani, L. Sun, Y. B. Zhang, T. S. Li, J. Kim, C. Y. Chim, G. Galli and F. Wang, *Nano Lett*, 2010, **10**, 1271–1275.

10 B. Radisavljevic, A. Radenovic, J. Brivio, V. Giacometti and A. Kis, *Nat. Nanotechnol.*, 2011, **6**, 147–150.

11 D. Xiao, G. B. Liu, W. X. Feng, X. D. Xu and W. Yao, *Phy. Rev. Lett.*, 2012, **108**, 196802.

12 H. L. Zeng, J. F. Dai, W. Yao, D. Xiao and X. D. Cui, *Nat. Nanotechnol.*, 2012, **7**, 490–493.

13 T. Cao, G. Wang, W. P. Han, H. Q. Ye, C. R. Zhu, J. R. Shi, Q. Niu, P. H. Tan, E. Wang, B. L. Liu and J. Feng, *Nat. Commun.*, 2012, **3**, 887.

14 K. F. Mak, K. L. He, J. Shan and T. F. Heinz, *Nat. Nanotechnol.*, 2012, **7**, 494–498.

15 K. F. Mak, K. L. McGill, J. Park and P. L. McEuen, *Science*, 2014, **344**, 1489–1492.

16 Y. J. Zhang, T. Oka, R. Suzuki, J. T. Ye and Y. Iwasa, *Science*, 2014, **344**, 725–728.

17 P. H. Tan, W. P. Han, W. J. Zhao, Z. H. Wu, K. Chang, H. Wang, Y. F. Wang, N. Bonini, N. Marzari, N. Pugno, G. Savini, A. Lombardo and A. C. Ferrari, *Nat. Mater.*, 2012, **11**, 294–300.

18 C. Lee, H. Yan, L. E. Brus, T. F. Heinz, J. Hone and S. Ryu, *ACS Nano*, 2010, **4**, 2695–2700.

19 X. Zhang, W. P. Han, J. B. Wu, S. Milana, Y. Lu, Q. Q. Li, A. C. Ferrari and P. H. Tan, *Phys. Rev. B*, 2013, **87**, 115413.

20 Y. Y. Zhao, X. Luo, H. Li, J. Zhang, P. T. Araujo, C. K. Gan, J. Wu, H. Zhang, S. Y. Quek, M. S. Dresselhaus and Q. H. Xiong, *Nano Lett.*, 2013, **13**, 1007–1015.

21 S. Najmaei, Z. Liu, W. Zhou, X. L. Zou, G. Shi, S. D. Lei, B. I. Yakobson, J. C. Idrobo, P. M. Ajayan and J. Lou, *Nat. Mater.*, 2013, **12**, 754–759.

22 G. Eda, H. Yamaguchi, D. Voiry, T. Fujita, M. Chen and M. Chhowalla, *Nano Lett.*, 2011, **11**, 5111–5116.

23 S. N. Shirodkar and U. V. Waghmare, *Phys. Rev. Lett.*, 2014, **112**, 157601.

24 L. F. Mattheiss, *Phys. Rev. B*, 1973, **8**, 3719–3740.

25 S. J. Sandoval, D. Yang, R. F. Frindt and J. C. Irwin, *Phys. Rev. B*, 1991, **44**, 3955–3962.

26 W. J. Zhao, Z. Ghorannevis, L. Q. Chu, M. L. Toh, C. Kloc, P. H. Tan and G. Eda, *ACS Nano*, 2013, **7**, 791–797.

27 W. C. Jin, P. C. Yeh, N. Zaki, D. T. Zhang, J. T. Sadowski, A. Al-Mahboob, A. M. van der Zande, D. A. Chenet, J. I. Dadap, I. P. Herman, P. Sutter, J. Hone and R. M. Osgood, *Phys. Rev. Lett.*, 2013, **111**, 106801.

28 W. J. Zhao, R. M. Ribeiro, M. L. Toh, A. Carvalho, C. Kloc, A. H. C. Neto and G. Eda, *Nano Lett.*, 2013, **13**, 5627–5634.

29 N. Scheuschner, O. Ochedowski, A. M. Kaulitz, R. Gillen, M. Schleberger and J. Maultzsch, *Phys. Rev. B*, 2014, **89**, 125406.

30 T. Eknapakul, P. D. C. King, M. Asakawa, P. Buaphet, R. H. He, S. K. Mo, H. Takagi, K. M. Shen, F. Baumberger, T. Sasagawa, S. Jungthawan and W. Meevasana, *Nano Lett.*, 2014, **14**, 1312–1316.

31 Y. Zhang, T. R. Chang, B. Zhou, Y. T. Cui, H. Yan, Z. K. Liu, F. Schmitt, J. Lee, R. Moore, Y. L. Chen, H. Lin, H. T. Jeng, S. K. Mo, Z. Hussain, A. Bansil and Z. X. Shen, *Nat. Nanotechnol.*, 2014, **9**, 111–115.

32 K. Albe and A. Klein, *Phys. Rev. B*, 2002, **66**, 073413.

33 S. Tongay, J. Zhou, C. Ataca, K. Lo, T. S. Matthews, J. B. Li, J. C. Grossman and J. Q. Wu, *Nano Lett.*, 2012, **12**, 5576–5580.

34 T. Cheiwchanchamnangij and W. R. L. Lambrecht, *Phys. Rev. B*, 2012, **85**, 205302.

35 H. P. Komsa and A. V. Krasheninnikov, *Phys. Rev. B*, 2012, **86**, 241201.

36 A. Ramasubramaniam, *Phys. Rev. B*, 2012, **86**, 115409.

37 D. Y. Qiu, F. H. da Jornada and S. G. Louie, *Phys. Rev. Lett.*, 2013, **111**, 216805.

38 C. D. Spataru, S. Ismail-Beigi, L. X. Benedict and S. G. Louie, *Phys. Rev. Lett.*, 2004, **92**, 077402.

39 F. Wang, G. Dukovic, L. E. Brus and T. F. Heinz, *Science*, 2005, **308**, 838–841.

40 A. Chernikov, T. Berkelbach, H. Hill, A. Rigosi, Y. Li, O. Aslan, D. Reichman, M. Hybertsen and T. Heinz, *arXiv:1403.4270*, 2014.

41 B. Zhu, X. Chen and X. Cui, *arXiv:1403.5108*, 2014.

42 G. Wang, X. Marie, I. Gerber, T. Amand, D. Lagarde, L. Bouet, M. Vidal, A. Balocchi and B. Urbaszek, *arXiv:1404.0056*, 2014.

43 Z. Ye, T. Cao, K. Ol'Brien, H. Zhu, X. Yin, Y. Wang, S. G. Louie and X. Zhang, *Nature*, 2014, **513**, 214–218.

44 X. B. Yin, Z. L. Ye, D. A. Chenet, Y. Ye, K. O'Brien, J. C. Hone and X. Zhang, *Science*, 2014, **344**, 488–490.

45 K. S. Novoselov, D. Jiang, F. Schedin, T. J. Booth, V. V. Khotkevich, S. V. Morozov and A. K. Geim, *Proc. Natl Acad. Sci.*, 2005, **102**, 10451–10453.

46 V. Nicolosi, M. Chhowalla, M. G. Kanatzidis, M. S. Strano and J. N. Coleman, *Science*, 2013, **340**, 1420–1424.

47 M. M. Benameur, B. Radisavljevic, J. S. Heron, S. Sahoo, H. Berger and A. Kis, *Nanotechnology*, 2011, **22**, 125706.

48 H. Li, J. M. T. Wu, X. Huang, G. Lu, J. Yang, X. Lu, Q. H. Zhang and H. Zhang, *Acs Nano*, 2013, **7**, 10344–10353.

49 R. J. Smith, P. J. King, M. Lotya, C. Wirtz, U. Khan, S. De, A. O'Neill, G. S. Duesberg, J. C. Grunlan, G. Moriarty, J. Chen, J. Wang, A. I. Minett, V. Nicolosi and J. N. Coleman, *Adv. Mater.*, 2011, **23**, 3944–3948.

50 X. Li, W. Cai, J. An, S. Kim, J. Nah, D. Yang, R. Piner, A. Velamakanni, I. Jung, E. Tutuc, S. K. Banerjee, L. Colombo and R. S. Ruoff, *Science*, 2009, **324**, 1312–1314.

51 Y. H. Lee, X. Q. Zhang, W. J. Zhang, M. T. Chang, C. T. Lin, K. D. Chang, Y. C. Yu, J. T. W. Wang, C. S. Chang, L. J. Li and T. W. Lin, *Adv. Mater.*, 2012, **24**, 2320–2325.

52 K. K. Liu, W. J. Zhang, Y. H. Lee, Y. C. Lin, M. T. Chang, C. Su, C. S. Chang, H. Li, Y. M. Shi, H. Zhang, C. S. Lai and L. J. Li, *Nano Lett.*, 2012, **12**, 1538–1544.

53 N. Wakabayashi, H. G. Smith and R. M. Nicklow, *Phys. Rev. B*, 1975, **12**, 659–663.

54 A. Molina-Sanchez and L. Wirtz, *Phys. Rev. B*, 2011, **84**, year.

55 G. Y. Zhang, G. X. Lan and Y. F. Wang, *Lattice Vibration Spectroscopy, 2nd ed.*, High Education Press, China, 1991.

56 J. L. Verble and T. J. Wieting, *Phys. Rev. Lett.*, 1970, **25**, 362–365.

57 C. Ataca, M. Topsakal, E. Akturk and S. Ciraci, *J. Phys. Chem. C*, 2011, **115**, 16354–16361.

58 J. Ribeiro-Soares, R. M. Almeida, E. B. Barros, P. T. Araujo, M. S. Dresselhaus, L. G. Cançado and A. Jorio, *arXiv:1407.1226*, 2014.

59 X. Luo, Y. Y. Zhao, J. Zhang, M. L. Toh, C. Kloc, Q. H. Xiong and S. Y. Quek, *Phys. Rev. B*, 2013, **88**, 195313.

60 J. L. Verble and T. J. Wieting, *Phys. Rev. Lett.*, 1970, **25**, 362–365.

61 T. J. Wieting and J. L. Verble, *Phys. Rev. B*, 1971, **3**, 4286–4292.

62 S. Horzum, H. Sahin, S. Cahangirov, P. Cudazzo, A. Rubio, T. Serin and F. M. Peeters, *Phys. Rev. B*, 2013, **87**, 125415.

63 H. Terrones, E. Del Corro, S. Feng, J. M. Poumirol, D. Rhodes, D. Smirnov, N. R. Pradhan, Z. Lin, M. A. T. Nguyen, A. L. Elias, T. E. Mallouk, L. Balicas, M. A. Pimenta and M. Terrones, *Sci. Rep.*, 2014, **4**, 4215.

64 Y. Q. Cai, J. H. Lan, G. Zhang and Y. W. Zhang, *Phys. Rev. B*, 2014, **89**, 035438.

65 A. Berkdemir, H. R. Gutierrez, A. R. Botello-Mendez, N. Perea-Lopez, A. L. Elias, C. I. Chia, B. Wang, V. H. Crespi, F. Lopez-Urias, J. C. Charlier, H. Terrones and M. Terrones, *Sci. Rep.*, 2013, **3**, 1755.

66 C. H. Chang, X. F. Fan, S. H. Lin and J. L. Kuo, *Phys. Rev. B*, 2013, **88**, 195420.

67 L. Liang and V. Meunier, *Nanoscale*, 2014, **6**, 5394–5401.

68 P. H. Tan, Z. Y. Xu, X. D. Luo, W. K. Ge, Y. Zhang, A. Mascarenhas, H. P. Xin and C. W. Tu, *Applied Physics Letters*, 2006, **89**, 101912.

69   G. L. Frey, R. Tenne, M. J. Matthews, M. S. Dresselhaus and G. Dresselhaus, *Phys. Rev. B*, 1999, **60**, 2883–2892.

70   R. Loudon, *Adv. Phys.*, 2001, **50**, 813–864.

71   E. Smith and G. Dent, in *The Theory of Raman Spectroscopy*, John Wiley & Sons, Ltd, 2005, pp. 71–92.

72   W. Zhao, Z. Ghorannevis, K. K. Amara, J. R. Pang, M. Toh, X. Zhang, C. Kloc, P. H. Tan and G. Eda, *Nanoscale*, 2013, **5**, 9677–9683.

73   X. Luo, Y. Y. Zhao, J. Zhang, Q. H. Xiong and S. Y. Quek, *Phys. Rev. B*, 2013, **88**, 075320.

74   P. Tonndorf, R. Schmidt, P. Böttger, X. Zhang, J. Börner, A. Liebig, M. Albrecht, C. Kloc, O. Gordan, D. R. T. Zahn, S. M. de Vasconcellos and R. Bratschitsch, *Opt. Express*, 2013, **21**, 4908–4916.

75   S. L. Li, H. Miyazaki, H. Song, H. Kuramochi, S. Nakaharai and K. Tsukagoshi, *ACS Nano*, 2012, **6**, 7381–7388.

76   G. Plechinger, J. Mann, E. Preciado, D. Barroso, A. Nguyen, J. Eroms, C. Schller, L. Bartels and T. Korn, *Semicond. Sci. Technol*, 2014, **29**, 064008.

77   G. Plechinger, S. Heydrich, J. Eroms, D. Weiss, C. Schller and T. Korn, *Appl. Phys. Lett.*, 2012, **101**, 101906.

78   H. L. Zeng, B. R. Zhu, K. Liu, J. H. Fan, X. D. Cui and Q. M. Zhang, *Phys. Rev. B*, 2012, **86**, 241301.

79   M. Boukhicha, M. Calandra, M. A. Measson, O. Lancry and A. Shukla, *Phys. Rev. B*, 2013, **87**, 195316.

80   P.-H. Tan, J.-B. Wu, W.-P. Han, W.-J. Zhao, X. Zhang, H. Wang and Y.-F. Wang, *Phys. Rev. B*, 2014, **89**, 235404.

81   J.-B. Wu, X. Zhang, M. Ij?s, W.-P. Han, X.-F. Qiao, X.-L. Li, D.-S. Jiang, A. C. Ferrari and P.-H. Tan, *Nat Commun*, 2014, **5**, 5309.

82   J. Zi, K. Zhang and X. Xie, *Phys. Rev. B*, 1997, **55**, 9263–9266.

83   S. Piscanec, M. Cantoro, A. C. Ferrari, J. A. Zapien, Y. Lifshitz, S. T. Lee, S. Hofmann and J. Robertson, *Phys. Rev. B*, 2003, **68**, 241312.

84   P. H. Tan, Y. Deng and Q. Zhao, *Phys. Rev. B*, 1998, **58**, 5435–5439.

85   E. H. Martins Ferreira, M. V. O. Moutinho, F. Stavale, M. M. Lucchese, R. B. Capaz, C. A. Achete and A. Jorio, *Phys. Rev. B*, 2010, **82**, 125429.

86   W. Shi, X. Zhang, X. L. Li, Q. Q. Li, J. B. Wu and P. H. Tan, *Unpublished*, 2014.

87   H. Richter, Z. P. Wang and L. Ley, *Solid State Commun.*, 1981, **39**, 625–629.

88   Y. Chen, D. O. Dumcenco, Y. Zhu, X. Zhang, N. Mao, Q. Feng, M. Zhang, J. Zhang, P.-H. Tan, Y.-S. Huang and L. Xie, *Nanoscale*, 2014, **6**, 2833–2839.

89   H.-P. Komsa and A. V. Krasheninnikov, *J. Phys. Chem. Lett.*, 2012, **3**, 3652–3656.

90   J. Kang, S. Tongay, J. Li and J. Wu, *J. Appl. Phys.*, 2013, **113**, 143703.

91   Y. Chen, J. Xi, D. O. Dumcenco, Z. Liu, K. Suenaga, D. Wang, Z. Shuai, Y.-S. Huang and L. Xie, *ACS Nano*, 2013, **7**, 4610–4616.

92   J. Mann, Q. Ma, P. M. Odenthal, M. Isarraraz, D. Le, E. Preciado, D. Barroso, K. Yamaguchi, G. V. Palacio, A. Nguyen, T. Tran, M. Wurch, A. Nguyen, V. Klee, S. Bobek, D. Z. Sun, T. F. Heinz, T. S. Rahman, R. Kawakami and L. Bartels, *Adv. Mater.*, 2014, **26**, 1399–1404.

93   C. Ramkumar, K. P. Jain and S. C. Abbi, *Phys. Rev. B*, 1996, **54**, 7921–7928.

94   D. O. Dumcenco, K. Y. Chen, Y. P. Wang, Y. S. Huang and K. K. Tiong, *J. Alloy. Compd.*, 2010, **506**, 940–943.

95   M. Zhang, J. Wu, Y. Zhu, D. O. Dumcenco, J. Hong, N. Mao, S. Deng, Y. Chen, Y. Yang, C. Jin, S. H. Chaki, Y.-S. Huang, J. Zhang and L. Xie, *ACS Nano*, 2014, **8**, 7130–7137.

96   K. Golasa, M. Grzeszczyk, P. Leszczynski, C. Faugeras, A. A. L. Nicolet, A. Wysmolek, M. Potemski and A. Babinski, *Appl. Phys. Lett.*, 2014, **104**, 092106.

97   J. M. Chen and C. S. Wang, *Solid State Commun.*, 1974, **14**, 857–860.

98   T. Sekine, K. Uchinokura, T. Nakashizu, E. Matsuura and R. Yoshizaki, *J. Phys. Soc. Jpn.*, 1984, **53**, 811–818.

99   T. Livneh and E. Sterer, *Phys. Rev. B*, 2010, **81**, 195209.

100   A. M. Stacy and D. T. Hodul, *Journal of Physics and Chemistry of Solids*, 1985, **46**, 405–409.

101   J. H. Fan, P. Gao, A. M. Zhang, B. R. Zhu, H. L. Zeng, X. D. Cui, R. He and Q. M. Zhang, *J. Appl. Phys.*, 2014, **115**, 053527.

102   J. R. Lince, S. V. Didziulis and J. A. Yarmoff, *Phys. Rev. B*, 1991, **43**, 4641–4647.

103   B. Windom, W. G. Sawyer and D. Hahn, *Tribology Letters*, 2011, **42**, 301–310.

104   L. F. Sun, J. X. Yan, D. Zhan, L. Liu, H. L. Hu, H. Li, B. K. Tay, J. L. Kuo, C. C. Huang, D. W. Hewak, P. S. Lee and Z. X. Shen, *Phys. Rev. Lett.*, 2013, **111**, 126801.

105   B. Chakraborty, H. Matte, A. K. Sood and C. N. R. Rao, *J. Raman Spectrosc.*, 2013, **44**, 92–96.

106   G. Sallen, L. Bouet, X. Marie, G. Wang, C. R. Zhu, W. P. Han, Y. Lu, P. H. Tan, T. Amand, B. L. Liu and B. Urbaszek, *Phys. Rev. B*, 2012, **86**, 081301.

107   A. C. Ferrari and D. M. Basko, *Nat. Nanotechnol.*, 2013, **8**, 235–246.

108   F. Cerdeira, E. Anastassakis, W. Kauschke and M. Cardona, *Phys. Rev. Lett.*, 1986, **57**, 3209–3212.

109   S. Bertolazzi, J. Brivio and A. Kis, *ACS Nano*, 2011, **5**, 9703–9709.

110   T. Korn, S. Heydrich, M. Hirmer, J. Schmutzler and C. Schuller, *Appl. Phys. Lett.*, 2011, **99**, 102109.

111   B. Chakraborty, A. Bera, D. V. S. Muthu, S. Bhowmick, U. V. Waghmare and A. K. Sood, *Phys. Rev. B*, 2012, **85**, 161403.

112   C. H. Chang, X. F. Fan, S. H. Lin and J. L. Kuo, *Phys. Rev. B*, 2013, **88**, 195420.

113   H. J. Conley, B. Wang, J. I. Ziegler, R. F. Haglund, S. T. Pantelides and K. I. Bolotin, *Nano Lett.*, 2013, **13**, 3626–3630.

114   M. Buscema, M. Barkelid, V. Zwiller, H. S. J. van der Zant, G. A. Steele and A. Castellanos-Gomez, *Nano Lett.*, 2013, **13**, 358–363.

115   D. Voiry, H. Yamaguchi, J. W. Li, R. Silva, D. C. B. Alves, T. Fujita, M. W. Chen, T. Asefa, V. B. Shenoy, G. Eda and M. Chhowalla, *Nat. Mater.*, 2013, **12**, 850–855.

116   C. R. Zhu, G. Wang, B. L. Liu, X. Marie, X. F. Qiao, X. Zhang, X. X. Wu, H. Fan, P. H. Tan, T. Amand and B. Urbaszek, *Phys. Rev. B*, 2013, **88**, 121301.

117   J. S. Ross, S. F. Wu, H. Y. Yu, N. J. Ghimire, A. M. Jones, G. Aivazian, J. Q. Yan, D. G. Mandrus, D. Xiao, W. Yao and X. D. Xu, *Nat. Commun.*, 2013, **4**, 1474.

118   J. S. Ross, P. Klement, A. M. Jones, N. J. Ghimire, J. Q. Yan, D. G. Mandrus, T. Taniguchi, K. Watanabe, K. Kitamura, W. Yao, D. H. Cobden and X. D. Xu, *Nat. Nanotechnol.*, 2014, **9**, 268–272.

119   A. A. Mitioglu, P. Plochocka, J. N. Jadczak, W. Escoffier, G. L. J. A. Rikken, L. Kulyuk and D. K. Maude, *Phys. Rev. B*, 2013, **88**, 245403.

120   Z.-H. Chi, X.-M. Zhao, H. Zhang, A. F. Goncharov, S. S. Lobanov, T. Kagayama, M. Sakata and X.-J. Chen, *Phys. Rev. Lett.*, 2014, **113**, 036802.

121   H. Sahin, S. Tongay, S. Horzum, W. Fan, J. Zhou, J. Li, J. Wu and F. M. Peeters, *Phys. Rev. B*, 2013, **87**, 165409.

122   Y. L. Wang, C. X. Cong, C. Y. Qiu and T. Yu, *Small*, 2013, **9**, 2857–2861.

123   M. Ghorbani-Asl, N. Zibouche, M. Wahiduzzaman, A. F. Oliveira, A. Kuc and T. Heine, *Sci. Rep.*, 2013, **3**, 2961.

124   N. A. Lanzillo, A. Glen Birdwell, M. Amani, F. J. Crowne, P. B. Shah, S. Najmaei, Z. Liu, P. M. Ajayan, J. Lou, M. Dubey, S. K. Nayak, apos and T. P. Regan, *Appl. Phys. Lett.*, 2013, **103**, 093102.

125   R. Yan, J. R. Simpson, S. Bertolazzi, J. Brivio, M. Watson, X. Wu, A. Kis, T. Luo, A. R. Hight Walker and H. G. Xing, *ACS Nano*, 2014, **8**, 986–993.

126   M. Thripuranthaka, R. V. Kashid, C. S. Rout and D. J. Late, *Appl. Phys. Lett.*, 2014, **104**, 081911.

127 M. Thripuranthaka and D. J. Late, *Acs Appl. Mater. Inter.*, 2014, **6**, 1158–1163.

128 D. J. Late, S. N. Shirodkar, U. V. Waghmare, V. P. David and C. N. R. Rao, *ChemPhysChem*, 2014, **15**, 1592–1598.

129 P. H. Tan, Y. Deng and Q. Zhao, *Phys. Rev. B*, 1998, **58**, 5435–5439.

130 S. Najmaei, Z. Liu, P. M. Ajayan and J. Lou, *Appl. Phys. Lett.*, 2012, **100**, 013106.

131 J. Menéndez and M. Cardona, *Phys. Rev. B*, 1984, **29**, 2051–2059.

132 P. H. Tan, Y. M. Deng, Q. Zhao and W. C. Cheng, *Appl. Phys. Lett.*, 1999, **74**, 1818–1820.

133 A. Taube, J. Judek, C. Jastrzebski, A. Duzynska, K. Switkowski and M. Zdrojek, *Acs Appl. Mater. Inter.*, 2014, **6**, 8959–8963.

134 L. Su, Y. Zhang, Y. Yu and L. Cao, *Nanoscale*, 2014, **6**, 4920–4927.

135 S. Sahoo, A. P. S. Gaur, M. Ahmadi, M. J.-F. Guinel and R. S. Katiyar, *J. Phys. Chem. C*, 2013, **117**, 9042–9047.

136 A. A. Balandin, S. Ghosh, W. Bao, I. Calizo, D. Teweldebrhan, F. Miao and C. N. Lau, *Nano Lett.*, 2008, **8**, 902–907.

137 Y. Cai, J. Lan, G. Zhang and Y.-W. Zhang, *Phys. Rev. B*, 2014, **89**, 035438.

138 B. D. Kong, S. Paul, M. B. Nardelli and K. W. Kim, *Phys. Rev. B*, 2009, **80**, 033406.

139 D. Yoon, Y.-W. Son and H. Cheong, *Nano Lett.*, 2011, **11**, 3227–3231.

140 J. Yan, Y. Zhang, P. Kim and A. Pinczuk, *Phys. Rev. Lett.*, 2007, **98**, 166802.

141 S. Pisana, M. Lazzeri, C. Casiraghi, K. S. Novoselov, A. K. Geim, A. C. Ferrari and F. Mauri, *Nat. Mater.*, 2007, **6**, 198–201.

142 M. Buscema, G. Steele, H. van der Zant and A. Castellanos-Gomez, *Nano Research*, 2014, **7**, 1–11.

143 L. Su, Y. Zhang, Y. Yu and L. Cao, *Nanoscale*, 2014, **6**, 4920–7.

144 S. Sugai and T. Ueda, *Phys. Rev. B*, 1982, **26**, 6554–6558.

145 L. Hromadová, R. Martoňák and E. Tosatti, *Phys. Rev. B*, 2013, **87**, 144105.

146 H. Guo, T. Yang, P. Tao, Y. Wang and Z. Zhang, *J. Appl. Phys.*, 2013, **113**, 013709.

147 C. Espejo, T. Rangel, A. H. Romero, X. Gonze and G.-M. Rignanese, *Phys. Rev. B*, 2013, **87**, 245114.

148 A. P. Nayak, S. Bhattacharyya, J. Zhu, J. Liu, X. Wu, T. Pandey, C. Jin, A. K. Singh, D. Akinwande and J.-F. Lin, *Nat Commun*, 2014, **5**, 3731.

149 P. Blake, E. W. Hill, A. H. Castro Neto, K. S. Novoselov, D. Jiang, R. Yang, T. J. Booth and A. K. Geim, *Appl. Phys. Lett.*, 2007, **91**, 063124.

150 Z. H. Ni, H. M. Wang, J. Kasim, H. M. Fan, T. Yu, Y. H. Wu, Y. P. Feng and Z. X. Shen, *Nano Lett.*, 2007, **7**, 2758–2763.

151 W. J. Zhao, P. H. Tan, J. Zhang and J. Liu, *Phys. Rev. B*, 2010, **82**, 245423.

152 K. Fukuda, K. Akatsuka, Y. Ebina, R. Ma, K. Takada, I. Nakai and T. Sasaki, *ACS Nano*, 2008, **2**, 1689–1695.

153 P. Nemes-Incze, Z. Osvath, K. Kamaras and L. P. Biro, *Carbon*, 2008, **46**, 1435–1442.

154 F. Tuinstra and J. L. Koenig, *J. Chem. Phys.*, 1970, **53**, 1126–1130.

155 R. J. Nemanich and S. A. Solin, *Phys. Rev. B*, 1979, **20**, 392–401.

156 A. C. Ferrari, J. C. Meyer, V. Scardaci, C. Casiraghi, M. Lazzeri, F. Mauri, S. Piscanec, D. Jiang, K. S. Novoselov, S. Roth and A. K. Geim, *Phys. Rev. Lett.*, 2006, **97**, 187401.

157 S. Reich, C. Thomsen and J. Maultzsch, *Carbon Nanotubes: Basic Concepts and Physical Properties*, Wiley-VCH, 2005.

158 A. Jorio, M. S. Dresselhaus, R. Saito and G. Dresselhaus, *Raman Spectroscopy in Graphene Related Systems*, Wiley-VCH, 2011.

159 Q. Y. Zhang, Y. C. Cheng, L. Y. Gan and U. Schwingenschlogl, *Phys. Rev. B*, 2013, **88**, 245447.

160 X. F. Qiao, X. L. Li, X. Zhang, W. Shi and P. H. Tan, *Unpublished*, 2014.

161 G. H. Li, A. Luican, J. M. B. L. dos Santos, A. H. C. Neto, A. Reina, J. Kong and E. Y. Andrei, *Nat. Phys.*, 2010, **6**, 109–113.

162 M. Yankowitz, J. Xue, D. Cormode, J. D. Sanchez-Yamagishi, K. Watanabe, T. Taniguchi, P. Jarillo-Herrero, P. Jacquod and B. J. LeRoy, *Nat Phys*, 2012, **8**, 382–386.

163 K. Kim, S. Coh, L. Z. Tan, W. Regan, J. M. Yuk, E. Chatterjee, M. F. Crommie, M. L. Cohen, S. G. Louie and A. Zettl, *Phys. Rev. Lett.*, 2012, **108**, 246103.

164 G. Trambly de Laissardiere, D. Mayou and L. Magaud, *Nano Lett.*, 2010, **10**, 804–808.

165 K. S. Novoselov, E. McCann, S. V. Morozov, V. I. Fal'ko, M. I. Katsnelson, U. Zeitler, D. Jiang, F. Schedin and A. K. Geim, *Nat. Phys.*, 2006, **2**, 177–180.

166 A. Castellanos-Gomez, H. van der Zant and G. Steele, *Nano Res.*, 2014, **7**, 1–7.

167 K. Liu, L. Zhang, T. Cao, C. Jin, D. Qiu, Q. Zhou, A. Zettl, P. Yang, S. G. Louie and F. Wang, *Nat Commun*, 2014, **5**, 4966.

168 T. Jiang, H. Liu, D. Huang, S. Zhang, Y. Li, X. Gong, Y.-R. Shen, W.-T. Liu and S. Wu, *Nat Nano*, 2014, **9**, 825–829.

169 A. K. Geim and I. V. Grigorieva, *Nature*, 2013, **499**, 419–425.

170 S. Tongay, H. Sahin, C. Ko, A. Luce, W. Fan, K. Liu, J. Zhou, Y. S. Huang, C. H. Ho, J. Y. Yan, D. F. Ogletree, S. Aloni, J. Ji, S. S. Li, J. B. Li, F. M. Peeters and J. Q. Wu, *Nat. Commun.*, 2014, **5**, 3252.

171 P. Hu, J. Zhang, M. Yoon, X.-F. Qiao, X. Zhang, W. Feng, P. H. Tan, W. Zheng, J. Liu, X. Wang, J. Idrobo, D. Geohegan and K. Xiao, *Nano Res.*, 2014, **7**, 694–703.

172 D. S. Kong, W. H. Dang, J. J. Cha, H. Li, S. Meister, H. L. Peng, Z. F. Liu and Y. Cui, *Nano Let.*, 2010, **10**, 2245–2250.

173 J. Zhang, Z. Peng, A. Soni, Y. Zhao, Y. Xiong, B. Peng, J. Wang, M. S. Dresselhaus and Q. Xiong, *Nano Lett.*, 2011, **11**, 2407–2414.

174 F. Liu, H. Shimotani, H. Shang, T. Kanagasekaran, V. Zlyomi, N. Drummond, V. I. Falko and K. Tanigaki, *ACS Nano*, 2014, **8**, 752–760.

175 P. Hu, L. Wang, M. Yoon, J. Zhang, W. Feng, X. Wang, Z. Wen, J. C. Idrobo, Y. Miyamoto, D. B. Geohegan and K. Xiao, *Nano Lett.*, 2013, **13**, 1649–1654.

176 S. R. Tamalampudi, Y.-Y. Lu, R. Kumar U., R. Sankar, C.-D. Liao, K. Moorthy B., C.-H. Cheng, F. C. Chou and Y.-T. Chen, *Nano. Lett.*, 2014, **14**, 2800–2806.

177 S. D. Lei, L. H. Ge, S. Najmaei, A. George, R. Kappera, J. Lou, M. Chhowalla, H. Yamaguchi, G. Gupta, R. Vajtai, A. D. Mohite and P. M. Ajayan, *ACS Nano*, 2014, **8**, 1263–1272.

178 X. J. Wu, X. Huang, J. Q. Liu, H. Li, J. Yang, B. Li, W. Huang and H. Zhang, *Angew. Chem. Int. Ed.*, 2014, **53**, 5083–5087.

179 F. Bonaccorso, P. H. Tan and A. C. Ferrari, *ACS Nano*, 2013, **7**, 1838–1844.

180 S. Z. Butler, S. M. Hollen, L. Y. Cao, Y. Cui, J. A. Gupta, H. R. Gutierrez, T. F. Heinz, S. S. Hong, J. X. Huang, A. F. Ismach, E. Johnston-Halperin, M. Kuno, V. V. Plashnitsa, R. D. Robinson, R. S. Ruoff, S. Salahuddin, J. Shan, L. Shi, M. G. Spencer, M. Terrones, W. Windl and J. E. Goldberger, *ACS Nano*, 2013, **7**, 2898–2926.

181 X. Huang, C. L. Tan, Z. Y. Yin and H. Zhang, *Adv. Mater.*, 2014, **26**, 2185–2204.

182 K. Chang and W. X. Chen, *ACS Nano*, 2011, **5**, 4720–4728.

183 J. Kang, J. Li, S.-S. Li, J.-B. Xia and L.-W. Wang, *Nano Lett.*, 2013, **13**, 5485–5490.

184 J. Kang, S. Tongay, J. Zhou, J. B. Li and J. Q. Wu, *Appl. Phys. Lett.*, 2013, **102**, 012111.

185 K. Kośmider and J. Fernández-Rossier, *Phys. Rev. B*, 2013, **87**, 075451.

186 H. Terrones, F. Lopez-Urias and M. Terrones, *Sci. Rep.*, 2013, **3**, 1549.

187 H. Fang, C. Battaglia, C. Carraro, S. Nemsak, B. Ozdol, J. S. Kang, H. A. Bechtel, S. B. Desai, F. Kronast, A. A. Unal, G. Conti, C. Conlon, G. K. Palsson, M. C. Martin, A. M. Minor, C. S. Fadley, E. Yablonovitch, R. Maboudian and A. Javey, *to be pulished in PNAS*, 2014.

188 S. Tongay, W. Fan, J. Kang, J. Park, U. Koldemir, J. Suh, D. S. Narang, K. Liu, J. Ji, J. Li, R. Sinclair and J. Wu, *Nano Lett.*, 2014, **14**, 3185–3190.

189 X. Hong, J. Kim, S.-F. Shi, Y. Zhang, C. Jin, Y. Sun, S. Tongay, J. Wu, Y. Zhang and F. Wang, *Nat. Nano.*, 2014, **9**, 682–686.

190 R. Cheng, D. Li, H. Zhou, C. Wang, A. Yin, S. Jiang, Y. Liu, Y. Chen, Y. Huang and X. Duan, *arXiv:1403.3447*, 2014.

191 W. Zhao, P. H. Tan, J. Liu and A. C. Ferrari, *J. Am. Chem. Soc.*, 2011, **133**, 5941–5946.

192 A. Castellanos-Gomez, H. van der Zant and G. Steele, *Nano Res.*, 2014, **7**, 1–7.

193 W. Dang, H. Peng, H. Li, P. Wang and Z. Liu, *Nano Lett.*, 2010, **10**, 2870–2876.

194 C. Cong and T. Yu, *Nat. Commun.*, 2014, **5**, 4709.

195 P. Moon and M. Koshino, *Phys. Rev. B*, 2013, **87**, 205404.